Wolfgang Helmut Lakata, BSc

A high repetition rate detection system for fs-non-linear and time-resolved spectroscopy

MASTER'S THESIS

to achieve the university degree of

Diplom-Ingenieur

Master's degree programme: Technical Physics

submitted to

Graz University of Technology

Supervisor

Koch, Markus, Assoc.Prof. Dipl.-Ing. Dr.techn.

in cooperation with Silicon Austria Labs GmbH

Graz, November 2020

Affidavit

I declare that I have authored this thesis independently, that I have not used other than the declared sources/resources, and that I have explicitly indicated all material which has been quoted either literally or by content from the sources used. The text document uploaded to TUGRAZonline is identical to the present master's thesis.

Date	Signature

Abstract

Capturing ultra fast processes like molecular vibrations are increasingly a topic of interest. Such fast events which occur at a timescale of $\sim$100 fs can be investigated by using pump-probe spectroscopy. This type of spectroscopy enables the possibility of studying ultrafast electronic dynamics.

Silicon Austria Labs (SAL) is currently building an ultra-short time laboratory which includes experiments with time resolved spectroscopy. This master's thesis is a pioneer work for SAL which covers planning, assembling and testing a single-beam pump-probe setup.

This thesis serves as preparation for a future implementation of a time-of-flight (ToF) camera as shot-to-shot measurement device in a spectrograph which enables the possibility of reducing the signal-to-noise ratio of the measured signal compared to other measuring methods.

Contents

List of Figures

1. Introduction

Spectroscopy is a valuable invention that is well-established for over 100 years now and is still used to do research on different interactions between electromagnetic radiation and matter. [29, 2]

1889 Arrhenius presented his work regarding the variation of chemical reactions with temperature. The Arrhenius equation 1.1 is used to describe the reaction rate $K(T)$ as a function of temperature T with the Boltzmann constant k_B and the activation energy E_a to start the chemical reaction and a prefactor A. [8]

$$K(T) = Ae^{-\frac{E_a}{k_B * T}} \tag{1.1}$$

In the 1920s flow and stopped flow experiments were implemented experimentally to follow chemical reactions with a millisecond timescale. In the 1930s scientists tried to understand atomic collisions and chemical reactions. Therefore a new theory was formulated by Eyring [33], Evans and Polanyi [13] called the transition state theory (TST). Therefore statistical mechanics was used to determine an expression for the prefactor A of the Arrhenius equation 1.1. The prefactor was evaluated to be in a range of 10^{13} Hz which is in the order of molecular vibrational frequencies. [8]

Due to the advances in laser technology, in particular regarding the intensity and repetition rate, over the last 50 years new phenomena appeared that do not vary linearly with the intensity any more. The non-linearity can be described as simultaneous interaction between multiple photons with a molecule. These effects are of significance to understand non-linear properties of materials induced by radiating molecules with intense laser light. Non-linear spectroscopy evolved hand in hand with non-linear optics and the progression can be divided into three periods. Between 1961 and

1965 several experiments were performed that rapidly revealed numerous non-linear effects. The second phase ranged from 1965 to 1969 and was mandatory for finding mathematical explanations for the previously discovered phenomena. This era was compulsory to form fundamentals for non-linear spectroscopy. In the early 1970s first tunable lasers were available that made it possible for spectroscopists to do research based on non-linear optics. [30, 5]

It took another decade until mid-1980s to develop femtosecond-lasers. Now it was possible to do real-time research on molecular motion. With these ultra short laser pulses Zewail started to observe dynamical processes like bond-breaking, bond-making and transitions with atomic scale resolution. For investigating an elementary chemical reaction Zewail took use of a method called flash photolysis in which an ultrafast laser pulse (pump-pulse) excites a system, in the meantime there is a second pulse called probe-pulse that evaluates the time evolution of the system at a certain time delay with respect to the pump pulse. His work was groundbreaking for probing atomic motions inside of molecules in real-time. [8, 27]

The aim of this Master's thesis is to build a single-beam pump-probe setup. The beam is therefore separated into two parts, a pump- and a probe-beam. The pump-beam is exciting the system while a probe beam is scanning the evolution of the system at different time delays. A significant difference between a conventional pump-probe setup and the planned system is the ultrafast detection mechanism. Therefore a grating spectrometer setup is used but for investigating ultrafast processes a time-of-flight (ToF) camera will be implemented into the system to detect the ultrafast spectrum. The ToF camera enables broadband shot-to-shot measurement which has the advantage to improve the signal-to-noise ratio drastically because of the intensity correlation of subsequent laser pulses. Another advantage that improves the signal-to-noise ratio is the measurement principle of the camera where pump- and pulse are read out at the same time. ToF cameras have two storage devices per pixel which can be switched very fast and therefore enable one readout for two storages. [18]

The thesis is split into several chapters beginning with an introduction, followed by fundamentals regarding pump-probe spectroscopy and the experimental setup, laser source and super-continuum generation followed by

pulse-length measurement, pulse-compression, pulse-chopping, spectrometer, evaluation of the specimen parameters and ends with the pump-probe experiment.

2. Pump-Probe Spectroscopy

For investigating ultra fast processes like molecular vibrations even faster events have to be used for capturing corresponding processes. The prefactor A of equation 1.1 states that ultrafast events like molecular vibrations occur at a periodic time in the range of $\sim$100 fs. Therefore femtosecond pulses are needed for gathering information about such effects. [8, 10]

First of all one has to trigger an event, therefore a strong pump-pulse is exciting a sample from its equilibrium state into a nonequilibrium state. Thereafter a relaxation process takes place back into its equilibrium state. For evaluating the whole process a weaker probe-pulse is used for capturing the process. The aim of a probe-pulse is to capture a change of an optical property ΔS like reflection or transmission without perturbing the process. For a time dependent signal one has to repeat the experiment at certain time delays τ_d to derive $\Delta S(\tau_d)$. The signal $\Delta S(\tau_d)$ is dependent of an interaction between light and matter. It is related to material specific parameters like occupation numbers, molecular orientations or charge carrier densities. [10]

2.1. Experimental Setup

The experimental setup can be seen in figure 2.1. For white light generation a 80 MHz fiberlaser which operates at 775 nm with 125 mW average power and 100 fs pulse-duration is separated with an 20/80 ultrafast beamsplitter. 80 % of the beam (orange path - probe) is transmitted and focused into a photonic crystal fiber (PCF) to generate a supercontinuum. Due to the use of a medium with high dispersion properties the spectral pulse length gets elongated by a certain amount and therefore the beam has to be temporally

compressed with a prismcompressor to maintain the temporal resolution. For delaying the signal a linear stage is used followed by an achromatic lens to focus into the sample and then analysed with a spectrograph. 20 % (red path - pump) of the beam is reflected and guided into a acousto-optical modulator (AOM) to perform pulse picking and finally focused into the sample. The last mirrors in front of the achromatic lens are used for adjustment to ensure a spatial overlap of pump and probe. In addition the pulse length can be evaluated with a interferometric autocorrelator (IAC) by flipping a mirror into the beam path (dashed lines).

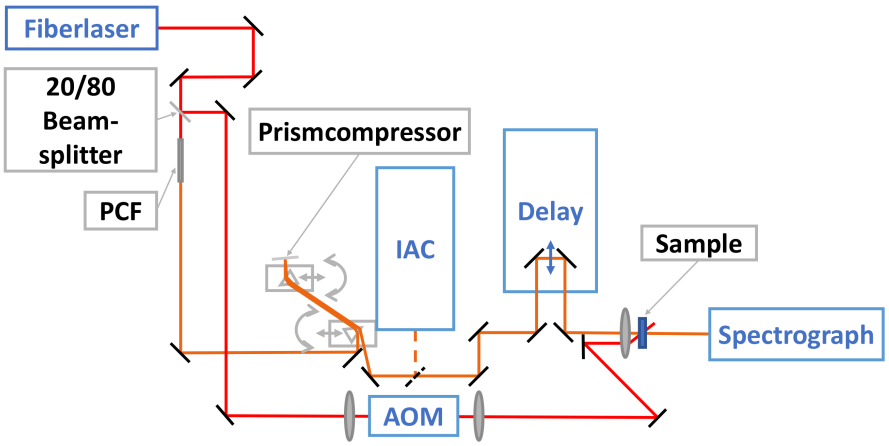

Figure 2.1.: Experimental setup: IAC...Interferometric-Auto-Correlator, AOM...Accousto-Optical-Modulator, Delay...Linear-Delaystage, PCF...Photonic-Crystal-Fiber, Orange-Lines...Probe-Beam, Red-Lines...Pump-Beam.

The idea is to generate a strongly broadened spectrum for the probe pulse to cover a wide range of frequencies for analyzing the sample at a repetition rate of 80 MHz. For pumping an AOM is used to pick every second pulse and therefore to derive a 40 MHz signal.

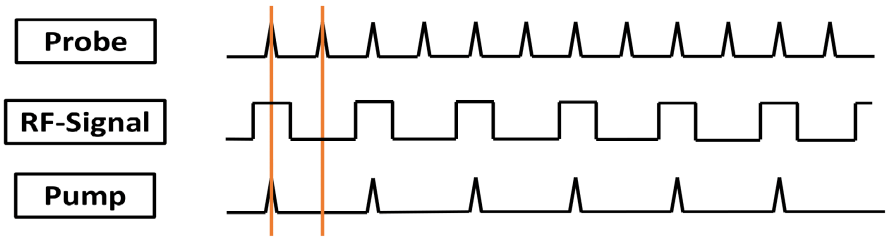

Figure 2.2.: Pump-Probe-Signal at Zero-Delay Position, Probe...Probe-Beam, RF-Signal...Radio-Frequency-Signal, Pump...Pump-Beam.

In figure 2.2 one can see the 80 MHz signal exiting the laser which is denoted as probe. An RF-signal is applied to the AOM which is synchronised with the output of the fiber laser. With the signal every second pulse is picked which yields to the pump signal. Pump- and probe-beams are then spatially overlapped in the sample point. This configuration above shows both pulses at zero delay. The probe-beam is then going to be delayed with respect to the pump-beam. However, the time evolution of the excitation is then analysed with the high repetition rate spectrograph.

3. Measurement Devices and Software

Table 3.1.: Devices used for the experiment, this includes the power-supply, laser-, calibration- and measuring-devices for evaluating average power, fast repetition rate processes, spectra, beam parameters and signals.

Device	Manufacturer	Identification
FS-Lasersource	TOPTICA	FemtoFiber pro NIR
Dual-Channel Powermeter	Newport	2832-C
Laboratory Powersupply	ISO-TECH	IPS 2303DD
Ultrafast Photodiode	THORLABS	DET210
Digital Oscilloscope	TELEDYNE LECROY	WavePro HD
Laserbeamprofiler	CINOGY	CinCAM 1.001-Nano
Spectrometer	AVANTES	AvaSpec-ULS3648
Calibrationlamp Ar-Hg	Mikropack	CAL-2000
Calibrationlamp Xenon-Arc	Oriel	/
Optical Microscope	Zeiss	Axio Imager
Digital Oscilloscope	Pico Technology	PicoScope 3206MSO
Lock-in Amplifier	STANFORD RESEARCH	MODEL SR830 DSP
Spectrophotometer	Agilent Technologies	Cary 60 UV-Vis

Table 3.1 represents the external devices used for the entire project. The fs-fiber-laser operates at 775 nm with a repetition rate of 80 MHz and a pulse-duration of 100 fs at a beam-size of 1.2 mm at $\frac{1}{e^2}$. For evaluating and plotting experimental data *Python* 3.7.4 was used. Raytracing and wavepropagation simulations were performed with *VirtualLabs Second Generation* provided by LightTrans. The PCF simulation was carried out with *Matlab* R2014a.

4. Lasersource and Super-Continuum Generation

Supercontinuum- (SC) or white light-generation is a significant topic since 1960 where non-linear effects were investigated and experimentally demonstrated. The effect appears if a narrow-band pulse is affected by a strong spectral non-linear broadening which produces a continuous output and was first under experimental research in the 1970s where bulk glass was used as non-linear medium. In the late 1990s photonic crystal fibers (PCF) were discovered as a new type of optical waveguide that were capable of generating broadband spectra with low energy laser pulses. Due to the flexibility in design of PCFs a variety of sources like cw-, fs- or ns- pulses can be used for spectral broadening. However, it is complicated to understand different contributions of physical effects like wave-mixing, self- and cross-phase modulation, soliton fission and Raman scattering that lead to SC generation in a particular case as a result of different fiber structures, pulse durations and energies. [11]

SC mechanisms can be divided into two classes regarding pulse duration: An ultrafast regime that deals with fs pulses and another that deals with slower input signals like nano-, pico-second and cw-sources. [11]

4.1. SC Generation in different media

4.1.1. Broadening in Bulk Materials

In 1970 white light was generated covering the visible part from 400 nm to 700 nm with 5 mJ pico-second pulses at 530 nm propagating through BK7

glass. This was the first time when spectral broadening was able to cover the entire visible spectrum. Until 2000 it was not possible to find an coherent explanation for SC-generation which changed by the first three-dimensional simulations of light propagation in bulk materials. SC generation in bulk materials occur due to the formation of an optical shock at the backside of the pulse because of self-steepening and space-time focusing. [11]

4.1.2. SC Generation in Fibers

White light generation in conventional fibers was performed in 1976 with high-power-, nanosecond-, kW-pulses in the visible region focusing into silica-fibers with a zero group velocity dispersion (GVD) of 1.3 µm. It was able to generate white light with 1.5 µm of bandwidth. The broadening can be attributed to self phase modulation (SPM) and Raman scattering. [11]

4.1.3. White-Light Generation in PCFs

In the mid 1970s assumptions were made to influence the guidance properties of fibers by implementing micro structures inside. It took another two decades until 1996 when there was a technological possibility to integrate small structures inside of fibers. Regarding SC-generation PCFs consist of a solid core in the center surrounded by an array of airholes extending lengthways along the fiber. However, the guidance property of such fibers arise due to internal reflection induced by a higher refractive index in the central region compared to the microstructure. Hole sizes and arrangement can be varied to adapt the guiding properties and dispersion which would be impossible for standard fibers. [11]

4.1.4. Electromagnetic Fields

An electromagnetic wave can be described as

$$E(z,t) = \tilde{E}(z,t)e^{i\alpha(\omega)z - i\omega t} + cc. \tag{4.1}$$

with $\tilde{E}(z,t)$ as the envelope of the field, α as propagation constant, z as position, ω as frequency, cc. as complex conjugate and t as time. [1]

The field in this thesis is always assumed to be gaussian and can be seen in equation 4.2 if nothing else is mentioned. [1]

$$\tilde{E}(t) = E_0 e^{-2\ln(2)\frac{t^2}{\tau_{fwhm}^2}} \tag{4.2}$$

where τ_{fwhm} is the full with at half maximum of the pulse duration. [1]

4.1.5. Wave Equation in Polarizable Materials

The wave equation of polarizable materials can be obtained from the Maxwell equations

$$-\frac{\partial^2}{\partial z^2}E(z,t) + \frac{1}{c^2}\frac{\partial^2 E(z,t)}{\partial t^2} = -\mu_0\frac{\partial^2 P(z,t)}{\partial t^2} \tag{4.3}$$

with $P(z,t)$ that is the induced polarization of the material. If the polarisation parameters are known one can solve equation 4.3 with different numeric algorithms. Therefore it is inevitable to introduce the susceptibility χ which is dependent of the material and describes how electromagnetic radiation induces a polarisation. [20]

Polarisation can be understood as interaction between electromagnetic radiation and charged particles. If we consider light in the visible part of the spectrum interacting with some molecules we get frequencies of $\sim 10^3$ THz which is too fast for atoms to follow, exclusively electrons are capable of being displaced from their equilibrium positions inducing an electric dipole moment

$$\mu(t) = -er(t) \tag{4.4}$$

where $r(t)$ is the time dependent displacement and e is the charge of an electron. [7]

4.1.6. Linear- and Nonlinear-Response

For weak electromagnetic fields, that means fields that are weaker than binding energies between electrons and nuclei, the displacement is linear to the electric field that yields to

$$P(t) = \epsilon_0 \chi E(t) \tag{4.5}$$

If the fields are stronger electrons are displaced further away from their equilibrium position and therefore the binding potential is not longer harmonic due to anharmonic terms that become more significant. In the case that anharmonic terms have to be taken into account the connection between electric field and polarisation is not linearly dependent any more. The polarisation can now be written as a power series

$$\begin{aligned} P(t) =& \epsilon_0 \left[\chi^{(1)} E(t) + \chi^{(2)} E(t)^2 + \chi^{(3)} E(t)^3 + ... \right] = \\ & P^{(1)}(t) + P^{(2)}(t) + P^{(3)}(t) + ... \end{aligned} \tag{4.6}$$

where $\chi^{(n)}$ is the nth order susceptibility and $P^{(n)}$ the contribution to the polarisation. [7]

4.1.7. Dispersion

For electromagnetic radiation propagating into matter one will observe a frequency dependent phase shift that is induced by cumulative material resonances. Dispersion can depicted with the frequency depending refractive index $n(\omega)$. One possible solution of the wave equation 4.3 is equation 4.1 with its propagation constant $\beta(\omega)$ at a central frequency ω_0. An arbitrary approach is to expand the propagation constant around its central frequency which yields to

$$\beta(\omega) = \beta_0 + \beta_1(\omega - \omega_0) + \frac{1}{2}\beta_2(\omega - \omega_0)^2 + ... \tag{4.7}$$

with $\beta_n = \frac{\partial^n \beta(\omega)}{\partial \omega^n}$. The first term describes the phase velocity $v_\Phi = \frac{\omega}{\beta_0}$ and can be interpreted as the propagation velocity of the electromagnet wavetop. Group velocity is described with the first order term $v_g = \beta_1^{-1}$ and can be understood as velocity of the pulse envelope. The second order term β_2 describes the group velocity dispersion (GVD) which causes chirp that is responsible for pulse stretching in time. [1]

4.1.8. Helmholtz Equation

A formulation in the frequency domain and three dimensions of equation 4.3 yields to the Helmholtz equation

$$\nabla^2 E(\mathbf{r}, \omega) = -\epsilon(\omega) \frac{\omega^2}{c^2} E(\mathbf{r}, \omega) \tag{4.8}$$

where $\epsilon(\omega) = 1 + \chi^{(1)}(\omega)$. Higher terms of $\chi^{(n)}$ can be implemented as perturbation. Equation 4.8 can be reformulated and treats pulse propagation in time space

$$\frac{\partial \tilde{E}}{\partial z} = i \left[\beta(\omega) - \beta_0\right] \tilde{E} + i\gamma |\tilde{E}|^2 \tilde{E} \approx \frac{1}{2} \beta_2 \frac{\partial^2}{\partial t^2} \tilde{E} + i\gamma |\tilde{E}|^2 \tilde{E} \tag{4.9}$$

with the non-linear coefficient $\gamma = \frac{n_2 \omega_0}{c A_{eff}}$ where n_2 is the nonlinear material index and A_{eff} the mode effective area.

4.1.9. Phase Modulation

All transparent and flat reflective media are able induce phase changes of a pulse without changing the spectral amplitude. Phase modulations are resulting from different phase delays of corresponding spectral components. We can now define an un-chirped pulse with

$$\tilde{E}(z, t) = \tilde{E}(0, t) e^{i\gamma |\tilde{E}(0,t)|^2 z} \tag{4.10}$$

where γ and $\tilde{E}(0,t)$ are responsible for phase and amplitude changes which is a solution of equation 4.9. The output pulse therefore has an additional phase change induced by the non-linear coefficient γ that leads to spectral broadening. If the pulse is responsible for the time variation the process is called self-phase modulation if extra pulses are responsible for changes of optical properties it is called cross-phase modulation. In many processes phase modulation appears if there is a temporal change of the refractive index n while pulse propagation. [1, 10]

4.1.10. Four-Wave Mixing and Raman Scattering

Four-wave mixing (FWM) is a process where three electromagnetic waves are interacting with each other to produce a fourth field. FWM can be understood when investigating different interactions of electromagnetic fields inside of a dielectric medium. The first field induces an oscillating polarisation which radiates phase shifted waves depending on the damping constant of the dipoles. A second field generates another polarisation, the two waves interfere and generate harmonics in the polarisation at the sum- and difference-frequencies. Basically the third field does the same with the first two fields as well as with the sum and difference frequencies while beating with sum and difference is the reason for generating a fourth field in the FWM process. There can be numerous interactions and fields driven by beat frequencies that can act as new fields. [31]

Raman scattering is defined as a particular type of light-matter interaction. Two light fields ω_1 and ω_2 at different frequencies are inducing oscillatory motions in the material at a difference frequency of $\Omega = \omega_1 - \omega_2$. The difference frequency Ω is low in comparison to ω_1 and ω_2 which enables resonance with vibrational modes ω_ν. [7]

4.1.11. Solitons

A solution of the pulse propagation equation 4.9 can be formulated as

$$\tilde{E}(z,t) = E_0 \text{sech}(\frac{2ln(1+\sqrt{2})t}{\tau_{fwhm}}) e^{i\frac{3.11|\beta_2|}{\tau^2_{fwhm}}z} \tag{4.11}$$

which can be easily proven by inserting. Equation 4.11 is a special type of pulse called fundamental soliton. Remarkably the pulse is able to propagate in time and space without distortion but there are more possible solutions for equation 4.9 but they are not stable over time and space. So called higher order solitons with order N can decay due to soliton fission into lower order solitons. Physically the pulses exist because of a balance between self-phase modulation and anomalous GVD for which we have $\beta_2 < 0$. Therefore a negative chirp is applied while self-phase modulation applies spectral broadening. The balance between these two effects can be understood as follows. If the pulselength is decreasing due to GVD SPM broadens the spectrum and increases the pulse stretching. The same explanation can be used if the pulselength is increasing therefore pulse stretching is decreasing and SPM broadens the spectrum. This working because SPM and spectral broadening lead to a positive chirp. [1]

4.2. SC-Simulation

Supercontinuum generation in optical fibers can be modelled with the non-linear generalized Schrödinger equation which will be solved in chapter 4.3 to perform a pulse-propagation simulation of the PCF. This yields to the non-linear propagation equation 4.12 that takes Kerr, dispersion, Raman scattering and self-steepening into account

$$\begin{aligned} &\frac{\partial A}{\partial z} + \beta_1 \frac{\partial A}{\partial t} + i\beta_2 \frac{\partial^2 A}{\partial t^2} - \beta_3 \frac{\partial^3 A}{\partial t^3} + ... = \\ &i\gamma(\omega) \left(1 + \frac{i}{\omega_0}\frac{\partial}{\partial t}\right) \left(A(z,t) \int_{-\infty}^{\infty} R(t') |A(z,t-t')|^2 dt'\right) \end{aligned} \tag{4.12}$$

where $R(t) = (1 - f_R)\delta(t) + f_R h_R(t)$, $A(z,t)$ is the envelope of the electric field, t is the delayed time for the envelope of the group velocity, β_i is the

taylor fit parameter of the dispersion relation at the carrier frequency ω_0, γ is the nonlinear coefficient of the fundamental mode and $0 < f_R < 1$ is the contribution of Raman response h_R which can be approximated by $h_R(t) \propto e^{-\frac{t}{\tau_2}} sin(\tau_1)$. [23]

A main disadvantage of equation 4.12 is that time discretization produces numerical errors and therefore a fourier transformation is advantageous that leads to

$$\begin{aligned} &\frac{\partial \tilde{A}}{\partial z} + i\tilde{A}\left(\beta(\Omega) - \beta_0 - \beta_1(\Omega)\right) = \\ &-i\gamma\left(1 + \frac{\Omega}{\omega_0}\right)\left(\mathcal{F}\left[(1-f_R)A|A|^2 + f_R A\mathcal{F}^{-1}\left[\tilde{h_R}\mathcal{F}\left[|A|^2\right]\right]\right]\right) \end{aligned} \tag{4.13}$$

with $\mathcal{F}$ as the fourier transformation, $\mathcal{F}^{-1}$ as inverse fourier transformation and symbols with tilde are also fourier transformed. To obtain a solution of equation 4.13 an adaptive step-size algorithm is used in which the step size h is adjusted in each iteration to reduce calculation time. [23]

4.3. Experimental Results

For supercontinuum generation a Toptica FemtoFiber pro laser that is operating at 80 MHz generates pulses with a temporal length of 100 fs at 775 nm, 124 mW average power and a beam diameter of 1.2 mm at $\frac{1}{e^2}$ is focusing into a Thorlabs NL-3.3-890-02 highly non-linear fiber with a non-linear coefficient of $\gamma = 37 \frac{1}{\mathrm{Wkm}}$. The photonic crystal fiber then guides the electromagnetic waves in a small solid silica core. A micro-structured cladding consisting of a periodic arrangement of air-holes in silica is surrounding the solid core and can be seen in figure 4.1. [3]

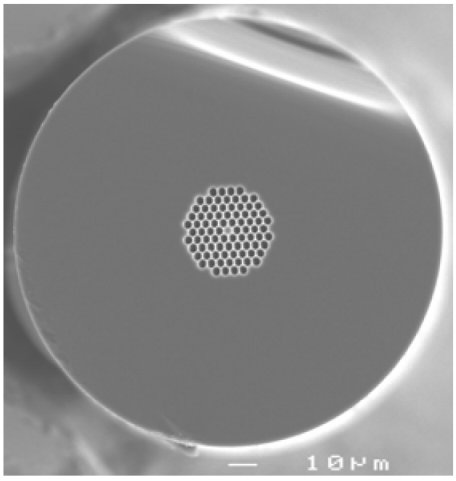

Figure 4.1.: Magnified cross-section of a Thorlabs NL-3.3-890-02 PCF. [3]

4.3.1. Simulation Data

For solving equation 4.11 one needs the fitparameters β_n of the dispersion plot that can be seen in figure 4.2.

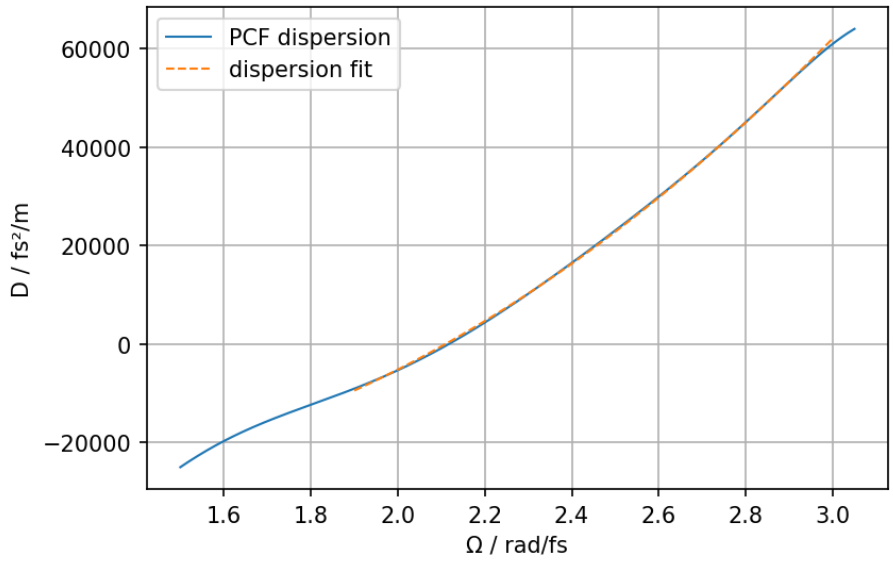

Figure 4.2.: Dispersion-data of Thorlabs NL-3.3-890-02 with Taylor-fit.

The dispersion plot is derived from the manufacturers datasheet and fitted according to equation 4.7 which yields to $\beta_2 = (17370 \pm 67)\,\frac{\mathrm{fs}^2}{\mathrm{m}}$, $\beta_3 = (63470 \pm 136)\,\frac{\mathrm{fs}^2}{\mathrm{m}}$ and $\beta_4 = (44886 \pm 965)\,\frac{\mathrm{fs}^2}{\mathrm{m}}$. In-coupling efficiency of the fiber was evaluated with the corresponding tool of *VirtualLabs* to determine the optimal lens for in-coupling into the PCF at a certain distance and a mode field diameter of (2.1 ± 0.1) µm which is the radius at which the intensity of the gaussian-beam decreases to $\frac{1}{e^2}$ [15]. The best result was evaluated with a Thorlabs C151TMB-B aspheric lens with a focal length of $f = 2.00\,\mathrm{mm}$, a numeric aperture of $NA = 0.5$ and anti reflection coating between $(600 - 1050)\,\mathrm{nm}$. The in-coupling lens was implemented into the setup after 60 cm behind the fiber laser with an ideal distance to the fiber of 3.34 mm resulting in an simulated maximal efficiency of 91 %. Therefore the average power was measured with the power-meter behind the lens to be 114 mW. For calculating the peak-power one has to determine the pulse-energy. This can be done with

$$E_{pulse} = \frac{P_{av}}{R_r} \tag{4.14}$$

where E_{pulse} is the pulse energy for a single pulse, P_{av} is the average power and R_r the repetition rate R_r of the laser system. An advantage of equation 4.14 is that the pulse-shape must not be taken into account. With the solution we can calculate the peak-power P_{max} for gaussian-beams

$$P_{max} = \frac{E_{pulse}}{\tau_p}\sqrt{\frac{2}{\pi}} \tag{4.15}$$

where τ_p is the pulse-duration which yields for $\tau_p = 100\,\text{fs}$ which was derived from the data-sheet and $P_{av} = 114\,\text{mW}$ with a repetition rate of $R_r = 80\,\text{MHz}$ to a peak-power of $P_{max} = 11.37\,\text{kW}$. Under consideration of 91% this would yield to $P_{max} = 10.35\,\text{kW}$ [12]

4.3.2. Fiber-Spectra

First a simulation was performed to determine the best fiber-length for spectral broadening which was done by solving equation 4.13 according to Rieznik et al. [23] with a corresponding *Matlab*-code. Therefore different fiber-lengths were simulated with the maximal peak power $P_{max} = 10.35\,\text{kW}$ as starting parameter. The simulation was done by increasing the simulated fiber-length after every execution of the simulation by 1 cm starting by 1 cm up to 15 cm and shows different spectra stacked over the others. This can be seen in figure 4.3 with normalized intensities.

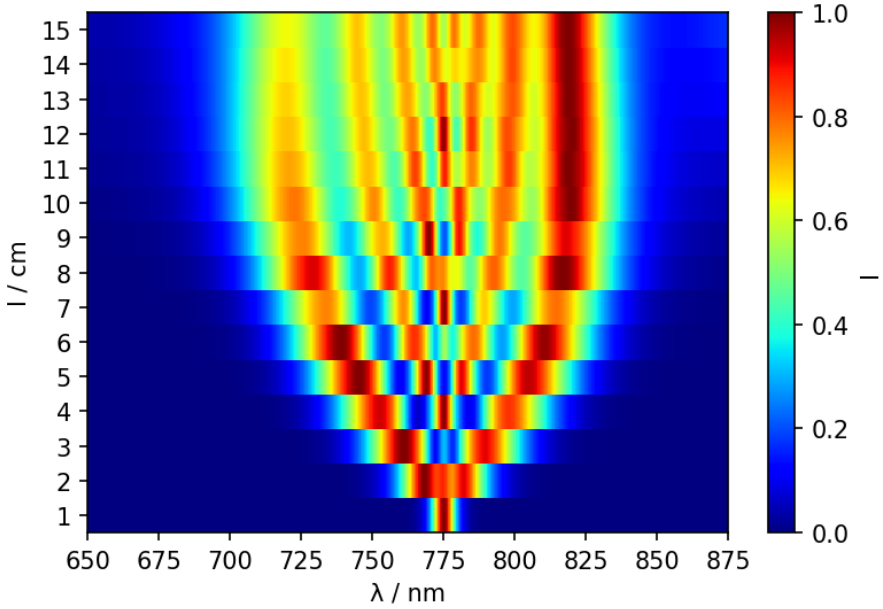

Figure 4.3.: Simulated dependency of the PCF spectrum on fiber-length with normalized intensities.

One can investigate that the spectrum is broadening until 8 cm to 10 cm of length and then stagnates.

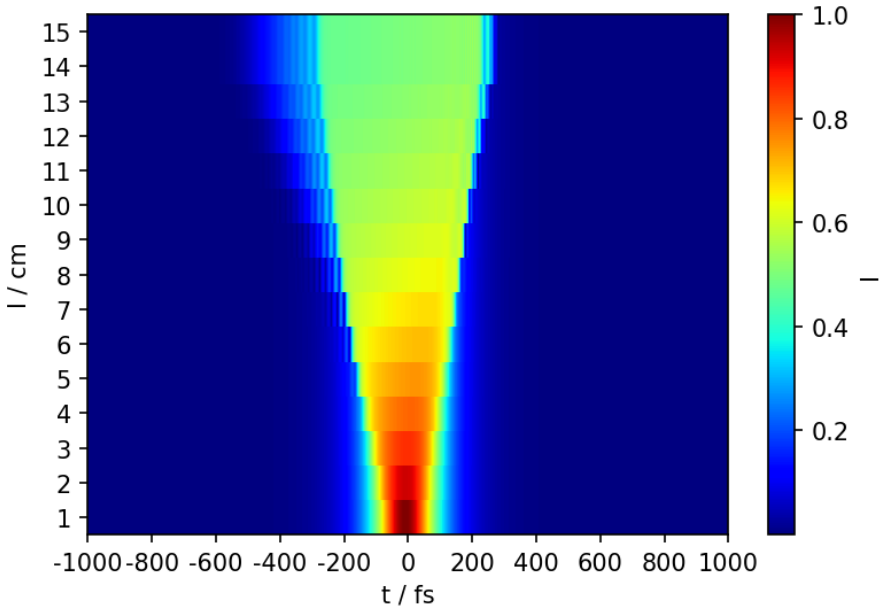

Figure 4.4.: Simulated dependency of the pulse-length with increasing fiber-length with normalized intensities.

Figure 4.4 shows how fiber-length variation influences the pulse duration. 15 simulations were performed with 1 cm step-size. It can be seen that the pulse-length increases continuously with increasing PCF-length.

Several spectra were simulated for evaluating the correct beam-splitter ratio between reflecting and transmitting due to separation in front of the PCF into pump- and probe-beam.

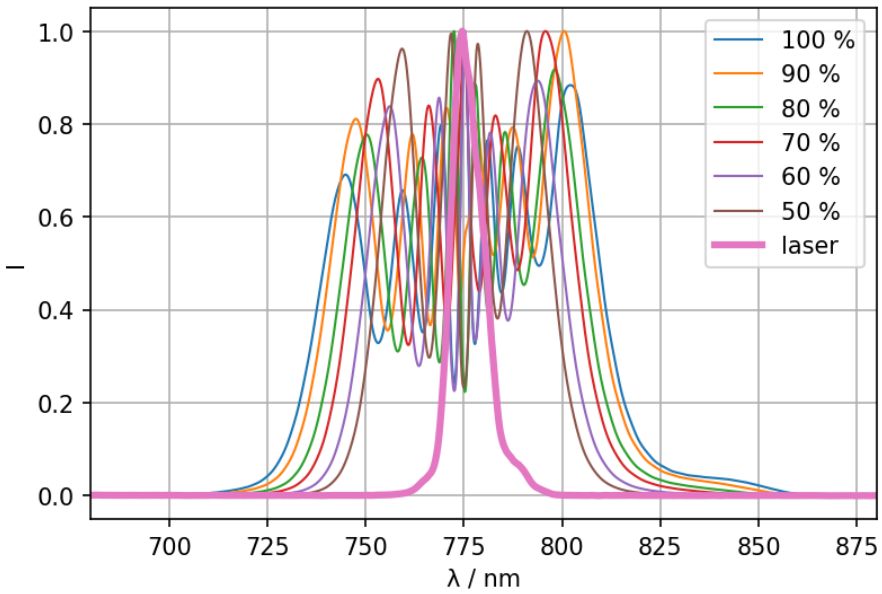

Figure 4.5.: Intensity normalized simulated PCF spectrum with $P_{max} = 10.35 = 100\,\%$, $P_{max} = 9.31\,\text{kW} = 90\,\%$, $P_{max} = 8.28\,\text{kW} = 80\,\%$, $P_{max} = 7.24\,\text{kW} = 70\,\%$,$P_{max} = 6.21\,\text{kW} = 60\,\%$,$P_{max} = 5.17\,\text{kW} = 50\,\%$.

In figure 4.5 one can see the simulated supercontinuum in dependency of the peak-input power. The laser-spectrum can be investigated at 775 nm represented by a thicker line which was previously recorded with the Avantes spectrometer. It can be seen that the spectrum is broadening linearly with increasing input power spanning a bandwidth of 100 nm from 720 nm to 820 nm with significant intensity. The spectrum is not fully symmetric around its central frequency, the right side, above 775 nm is broadening more than the left side below 775 nm.

4.3.3. Fiber Preparation

PCFs were usually delivered as fibers with a multiple length of one meter and therefore further processing is required to obtain the desired length of 8 cm. First step is to cleave the fiber which can be a delicate process to produce flat edges. Therefore a self-made fiber cleaving tool was used.

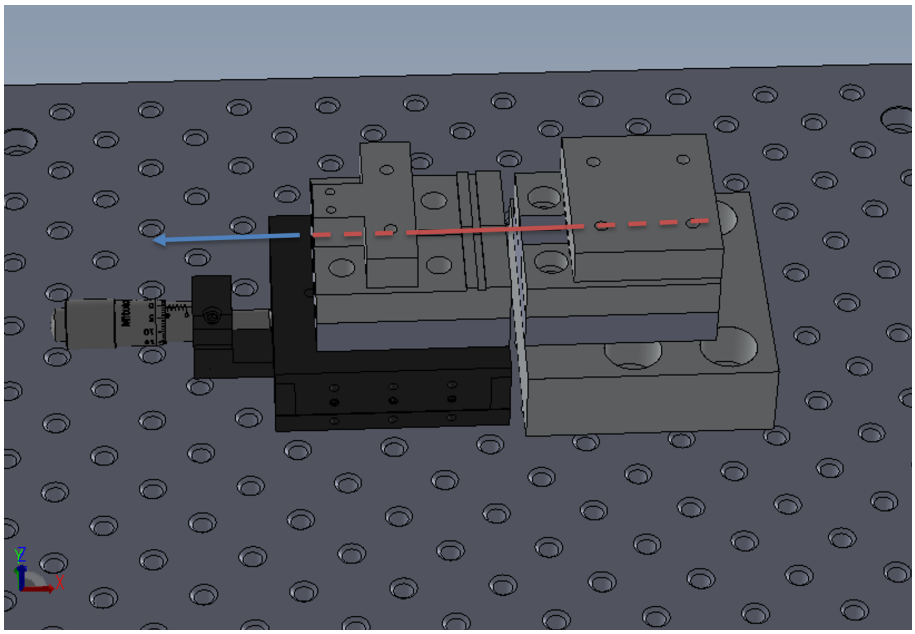

Figure 4.6.: Self-made fiber cleaving tool with symbolized fiber (red line) and blue arrow representing the direction of the tools translational movement.

Figure 4.6 shows the apparatus for cleaving. The red line represents the position of the PCF inside the tool while dashed lines show parts of the fiber clamped into the device. After fixing the PCF a force is applied with a translation stage which is represented by a blue arrow inducing stress to the fiber. If the stretching is tight enough a small scratch can be made with a ruby knife in the middle of the apparatus which results in a spontaneous fracture at the same spot. PCFs are usually protected with a lacquer coating around their entire length. That layer has to be removed before mounting it into the setup. This can be accomplished with a special fiber-stripper. The device acts exactly the same as a conventional wire-stripper but in a smaller scale. For investigating the result the optical-microscope from Zeiss was used. A transition between stripped and non-stripped fiber can be seen in figure 4.7.

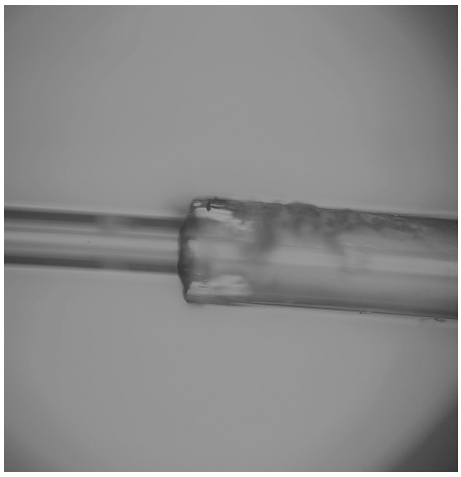

Figure 4.7.: Transition between stripped and non-stripped PCF at 100x magnification.

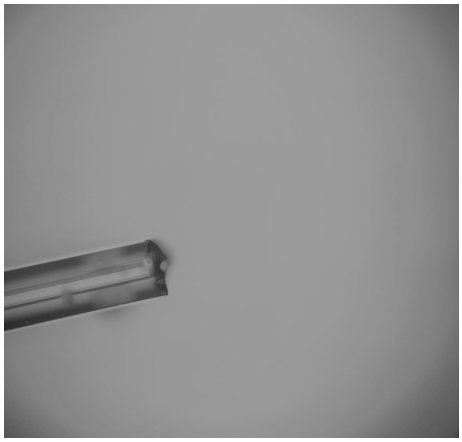

(a) PCF side a.

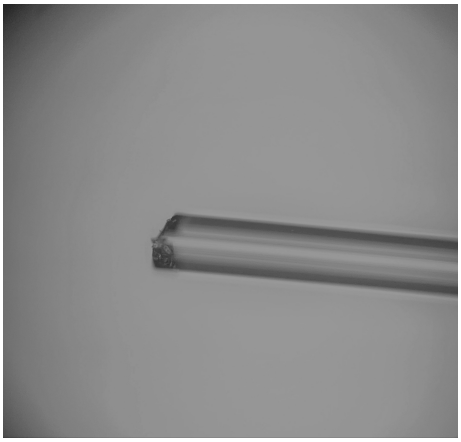

(b) PCF side b.

Figure 4.8.: Cleaved and stripped fiber endings at 100x magnification.

Figure 4.8 shows cleaved and stripped fiber endings while figure 4.8(a) shows a slightly smoother edge in comparison with figure 4.8(b) which can be suitable for better in-coupling. If one has a closer look at figure 4.8 in the middle of the PCF the microstructure can be adumbrated.

4.3.4. Test Results

For separating the laserbeam in front of PCF an ultrafast GDD beamsplitter should be used with available reflection and transmission ratios. Having a look at figure 4.5 reveals that 80 % transmission is sufficient for an adequate broadening.

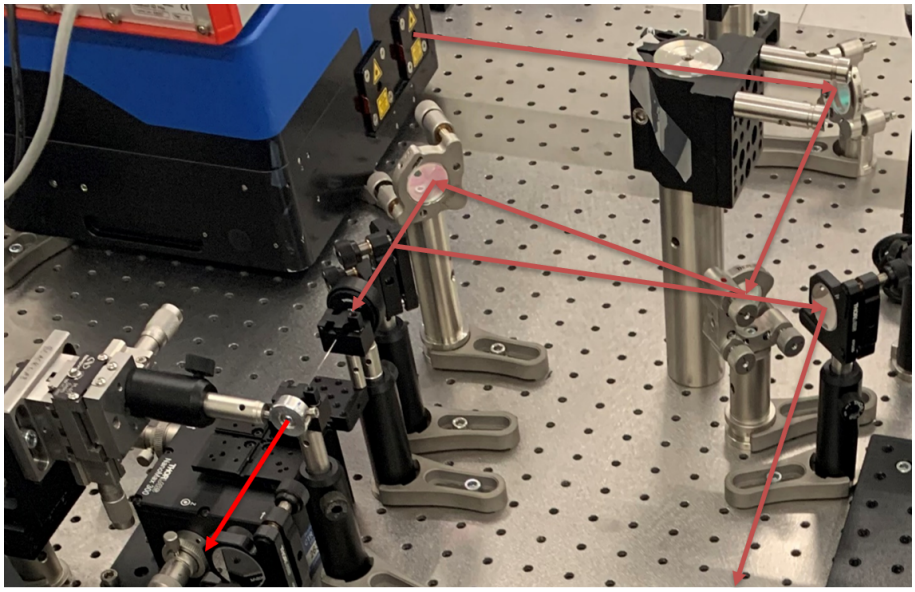

Figure 4.9.: Lasersource with beamsplitter and fiber in-coupling.

Figure 4.9 shows the laser beam exiting the fiber laser at the top-left corner and then extending the path-length with three dielectric mirrors. The beam is then separated at the low GDD beamsplitter. The probe beam is reflected and guiding into the right side and then reflected by another mirror. The pump-beam is focused with a 2 mm lens into the fiber and then collimated with a C390TME-B which has a slightly longer focal length compared to the in-coupling lens with 2.0 mm due to a relatively long beam path afterwards which makes it more comfortable to collimate properly with a focal length of 2.75 mm. The lens is mounted on a 3d-stage for better alignment. In figure 4.9 it can be seen that the PCF is mounted on a 3-axis nano stage to ensure a proper alignment of the fiber on the in-coupling

side. It is a relatively delicate process to align lens and PCF for maximum efficiency and best possible broadening due to the small mode-field diameter. Therefore the beamsplitter was inserted before a measurement at maximum intensity was performed because of a beam-displacement that would require a readjustment of the setup.

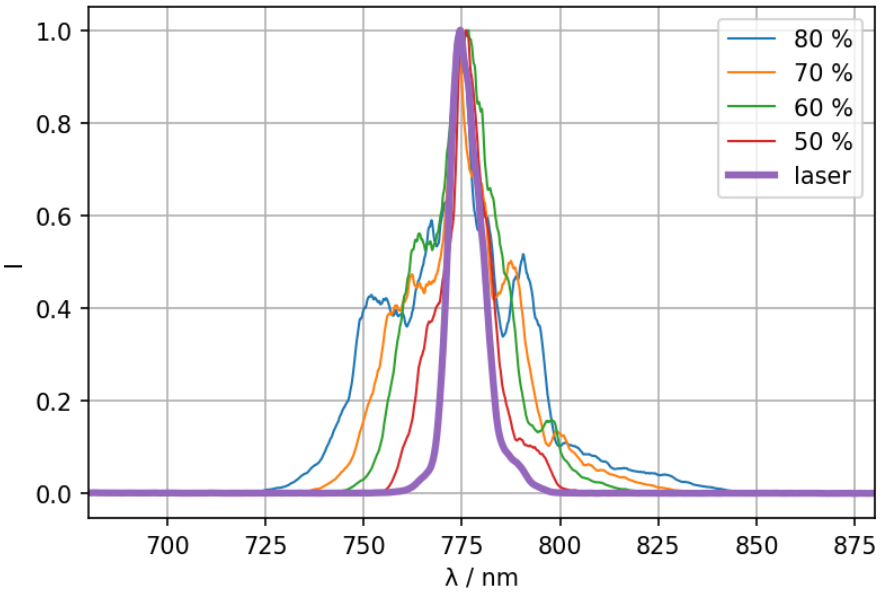

Figure 4.10.: Broadened, normalized and Savitzky-Golay filtered spectrum after PCF with variation of the input power in 10 % steps beginning with 80 % of the maximum power withouth beamsplitter.

A measurement with the powermeter showed that 92 mW were exiting the in-coupling lens and 67 mW can be obtained after broadening behind the PCF that yields to 73 % efficiency. A continuous neutral-density filter was used to vary the input power of 92 mW in 10 % steps which yields to 80 % of the maximum that would be in-coupled into the PCF without beamsplitter. The results can be seen in figure 4.10. According to equation 4.15 67 mW correspond to 6.682 kW of peak power.

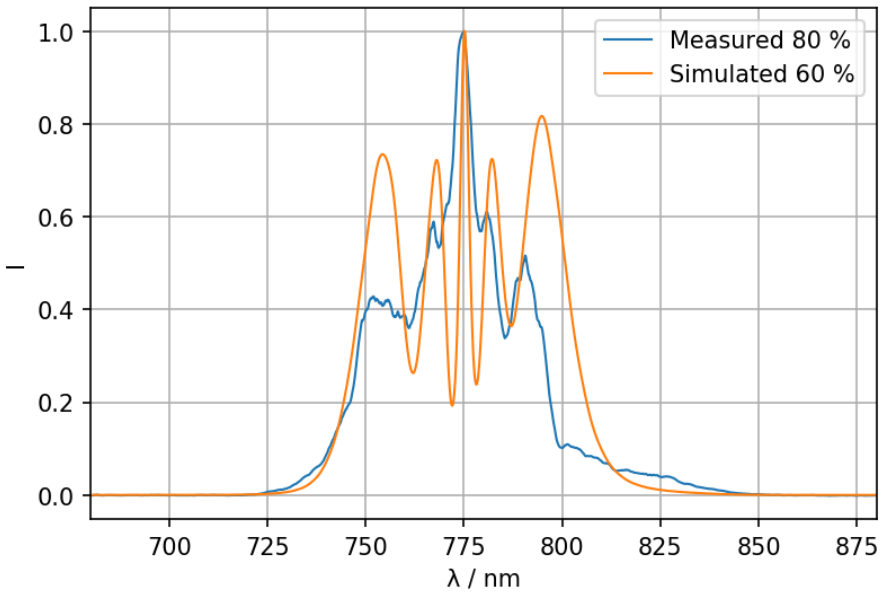

Figure 4.11.: Normalized measured and Savitzky-Golay filtered spectrum behind beam-splitter compared with simulated spectrum with adjusted peak power of $P_{max} = 6.682\,\mathrm{kW}$.

Figure 4.11 shows the comparison between simulated and measured super-continuum spectrum. It can be seen that the peaks of simulated spectrum fit with the peaks of the measured one except the side above 775 nm differs a bit. The deviation may be explained due to semi-optimal in-coupling because of uneven surfaces caused by the cleaving process.

5. Pulse-Length Measurement

Electromagnetic radiation whether ultrashort pulses or continuous waves follow the rules of classical electromagnetic formulation but fs pulses are more delicate regarding their handling. A main parameter that influences time resolution in measurements is the pulse length. With increasing pulse-lengths temporal resolution decreases and vice versa. Therefore a main task is to maintain short pulses in order to investigate ultrafast events. The index of refraction is the parameter that influences pulselengths. As previously mentioned in chapter 4.1.7 the second derivative of refractive index is called group velocity dispersion (GVD) which is positive in the range of the visible spectrum for most transparent materials and results in a frequency dependent delay of spectral components. [10, 24]

5.1. Pulse Broadening

Transparent materials can be described with a fit of refractive indices as a function of wavelengths according to the Sellmeier equation [4]

$$n^2(\lambda) = 1 + \frac{B_1\lambda^2}{\lambda^2 - C_1} + \frac{B_2\lambda^2}{\lambda^2 - C_2} + \frac{B_3\lambda^2}{\lambda^2 - C_3} \tag{5.1}$$

In the case of SF10, a commonly used transparent material for pulse compression, we would derive according to equation 5.1 for a wavelength range of $\lambda = (450 - 900)$ µm

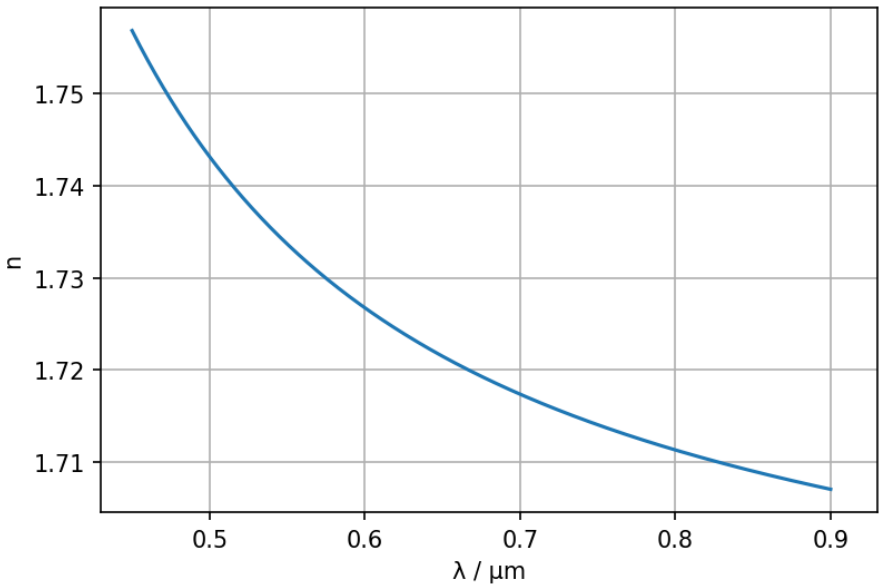

Figure 5.1.: Refractive index over wavelength of SF10.

with $B_1 = 1.62153902\,\frac{1}{\mu m^2}$, $B_2 = 0.256287842\,\frac{1}{\mu m^2}$, $B_3 = 1.64447552\,\frac{1}{\mu m^2}$, $C_1 = 0.0122241457\,\mu m^2$, $C_2 = 0.0595736775\,\mu m^2$, $C_3 = 147.468793\,\mu m^2$ according to the Schott [26] datasheet.

Derivatives of the refractive index with respect to the wavelength can be derived with the Sellmeier series expansion [4]

$$\frac{dn}{d\lambda} = -\frac{\lambda}{n}\sum_{i=1}^{3}\frac{B_i C_i^2}{\left(\lambda^2 - C_i^2\right)^2} \tag{5.2}$$

$$\frac{d^2n}{d\lambda^2} = \frac{1}{\lambda}\frac{dn}{d\lambda} - \frac{1}{n}\left(\frac{dn}{d\lambda}\right)^2 + \frac{4\lambda^2}{n}\sum_{i=1}^{3}\frac{B_i C_i^2}{\left(\lambda^2 - C_i^2\right)^3} \tag{5.3}$$

With equation 5.2 and 5.3 first- and second-derivative of the refractive index with respect to the wavelength can be plotted

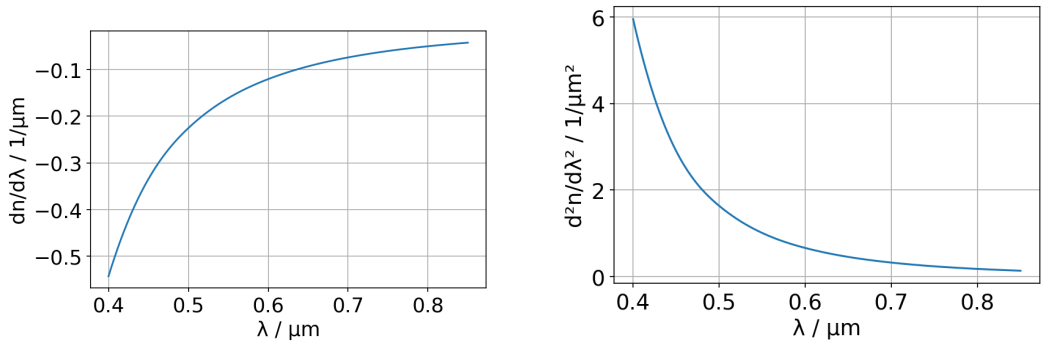

(a) First derivative.

(b) Second derivative.

Figure 5.2.: Derivatives of the refractive index with respect to the wavelength of SF10.

Figure 5.2(a) shows the propagation velocity while figure 5.2(b) represents the group velocity dispersion of SF10. It can be seen that different wavelengths travel with different velocities which results in a pulse deformation and therefore a temporal stretching. In other words shorter wavelengths travel slower than longer ones. [10]

It is advantageous to determine the pulselength in order to identify the temporal resolution of an experiment. Therefore direct measurements with semiconductor devices are not feasible because of their relatively low response times. A possibility is to use autocorrelation where the pulse is initially split with a beamsplitter. The first beam acts like a reference signal while the second beam is delayed. This process takes place in a conventional Michelson Morley interferometer (MMI) while the pulse is recombined in a non-linear material where two or three photons combine at the same time. A new signal can be observed while one beampath is varied with respect to the other which is called autocorrelation signal $I_{ac}(\tau)$. [24]

There are two relatively simple methods for quantifying the coherence of a light source. Therefore intensity autocorrelation (AC) or interferometric autocorrelation (IAC) can be used while IAC provides additional information regarding the phase which can be practical when characterizing ultrashort pulses. An advantage is that IAC and AC measure the fourth and second

power of the electric field amplitude which improves the contrast and sensitivity of the measurement. For pulsed light one has a peak-to-background ratio of 8:1 while AC has 2:0. Both measurements can be performed with second-harmonic generation in a non-linear crystal or two-photon absorption (TPA) in a semiconductor. The overlap between reference signal and delayed replica occurs in the non-linear crystal which results in a combination of two photons producing light with doubled frequency $I_{ac}(\tau)$

$$I_{ac}(\tau) = \int_{-\infty}^{\infty} \left| \left(E(t) + E(t+\tau)^2 \right) \right|^2 dt \tag{5.4}$$

where $E(t)$ is the reference signal and $E(t+\tau)$ the delayed replica. [32]

5.2. Setup and Measurement

The setup can be seen in figure 5.3 which consists of a Michelson Morley interferometer at the left side. The MMI splits the beam with a ultrafast low GDD beamsplitter and delays with a linear step-motorized stage. Both beams are focused with a parabolic mirror to prevent additional GVD into a beta barium borate (BBO) crystal which frequency doubles a fraction of both beams symbolized by blue arrows. Separation then is performed with a dichroic beam splitter into a highly sensitive avalanche photodiode with two blue filters to ensure that no light can enter the diode that is not frequency doubled. There is also a second photodiode for measuring the interferogram.

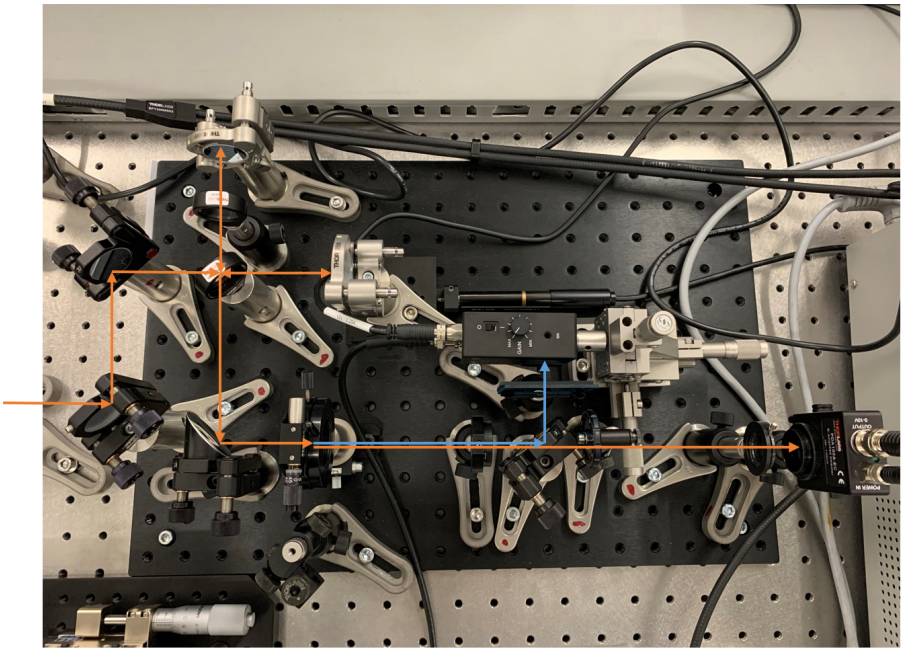

Figure 5.3.: Interferometric Autocorrelation setup.

At the start both beams have to be spatially overlapped which can be verified with the second photodiode. A tricky part is to adjust the BBO in such a way to gain maximum efficiency by second-harmonic generation where the crystal has to be in focus, tilted by the right amount around the optical axis and turned vertically to fulfil the phase matching condition.

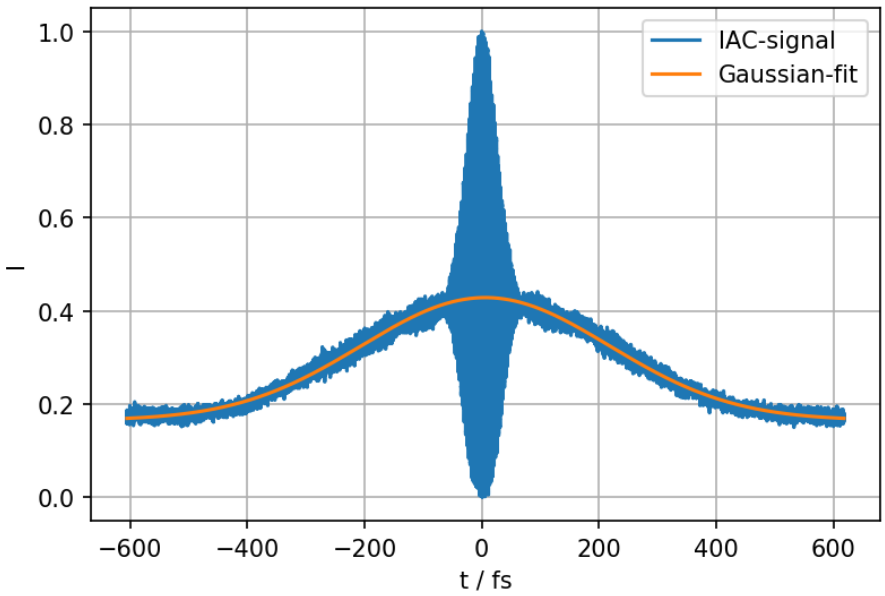

Figure 5.4.: Normalized interferometric autocorrelation of the uncompressed supercontinuum pulse with Gaussian-fit.

Figure 5.4 shows the intensity distribution of the uncompressed pulse after the PCF which is fitted with a Gaussian-fit. For determining of the pulse-length the intensity distribution plot is divided by $\sqrt{2}$ to derive the electric-field. The pulse-length is then evaluated to be $\tau_{fwhm,meas} = (423 \pm 7)\,\mathrm{fs}$ in temporal length at full-width at half maximum. The time axis must be calibrated which can be done by looking at two peaks of the oscillations. Peak-to-peak distance has to be $\frac{\lambda}{c}$ where $\lambda = 775\,\mathrm{nm}$ and c the speed of light.

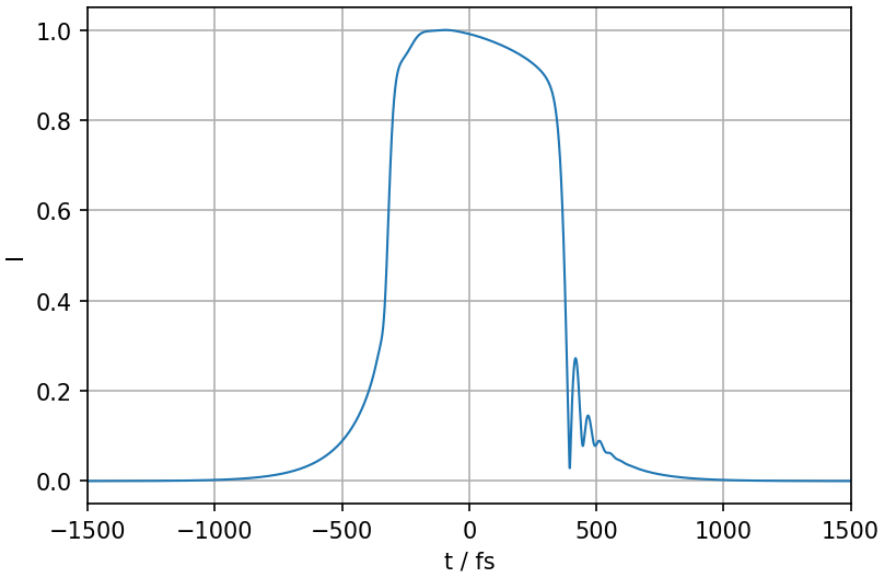

Figure 5.5.: Simulated pulselength with 8 cm PCF at 6.682 kW.

Another simulation was performed according to equation 4.13 regarding the pulse length at 8 cm of PCF length and 6.682 kW peak power. The result can be seen in figure 5.5 showing that the pulse length is $\tau_{fwhm,sim} = 443\,\text{fs}$ which is in the range of the measured pulse length.

Now simulated $\tau_{fwhm,sim} = 443\,\text{fs}$ and measured $\tau_{fwhm,meas} = (423 \pm 7)\,\text{fs}$ pulse-lengths can be compared. It can be seen that they do not match within the error calculation interval. This can be explained due to the measurement technique of the fiber-length which was roughly evaluated with a tape measure. If one has a look at figure 4.4 one can see that 1 cm of fiber-length increase adds $\sim 30\,\text{fs}$ of pulse time in the region around 8 cm. Considering the additional uncertainty to be in the range of 0.5 cm one can evaluate the measured pulse-length to be $\tau_{fwhm,meas} = (423 \pm 22)\,\text{fs}$ which fits with the simulated result.

6. Pulse-Compression

6.1. Dispersion effects on Ultrashort Pulses

According to equation 5.3 and figure 5.2b(b) one can see that transparent materials apply a positive GVD to a pulse resulting in temporal enlargement. However, for investigating dispersive effects on pulses equation 4.1 and 4.2 can be reformulated

$$\tilde{E}(t) = \sqrt{A_t e^{-\ln(2)(\frac{2t}{\Delta t})^2}} e^{-i(\omega_0 t + \theta(t))} + cc. \tag{6.1}$$

where A_t is the amplitude of the pulse, ω_0 the carrier frequency, Δt the minimum pulse duration, $\theta(t)$ the temporal relationship of the frequency components which describes the modification of the pulse-duration and $cc.$ is the complex conjugate. [9]

It can be problematic when solving integrals numerically in the time domain and therefore we transform equation 6.1 into the frequency domain by performing a Fourier transformation

$$\tilde{E}(\omega) = \sqrt{A_\omega e^{-\ln(2)(\frac{2(\omega-\omega_0)}{\Delta\omega})^2}} e^{-i\varphi_{pulse}(\omega-\omega_0)} \tag{6.2}$$

while $\Delta\omega$ and Δt are related through the uncertainty principle via $\Delta\omega\Delta t = 4\ln(2)$. Angular frequencies ω can not be measured but linear frequencies ν can, therefore the uncertainty principle becomes $c_B = \Delta\nu\Delta t = \frac{2\ln(2)}{\pi}$ for Gaussian beams and is dependent on the pulseshape. After propagation through dispersive media the pulse can be expressed as a product of the initial pulse $E_{in}(\omega)$ and a transfer function dependent of the material

$$E_{out}(\omega) = E_{in}(\omega)R(\omega)e^{-i\varphi_{mat}(\omega-\omega_0)} \tag{6.3}$$

where $\varphi_{Mat}(\omega - \omega_0)$ describes the additional phase and $R(\omega)$ is an amplitude scaling factor. [9]

The phase can be expressed as Taylor expansion around the carrier frequency ω_0

$$\varphi(\omega - \omega_0) = \varphi_0 + \varphi_1(\omega - \omega_0) + \varphi_2\frac{(\omega - \omega_0)^2}{2} + \varphi_3\frac{(\omega - \omega_0)^3}{3} + ... \tag{6.4}$$

Equation 6.4 enables a better comprehension of dispersion. The phase can be defined as $\phi(\omega) = k(\omega)L$ where $k(\omega)$ is the propagation constant and L the propagation length. It is already known that the group velocity is $v_g = \frac{d\omega}{dk}$. By inserting these properties into equation 6.4 it can be investigated that the first term adds a constant phase while the second term which is proportional to $\frac{1}{v_g}$ adds delay to the initial pulse while pulse shape is not affected. The third term is called group delay dispersion (GDD) and is proportional to $\frac{d}{d\omega}(\frac{1}{v_g})$ which is known as group velocity dispersion (GVD) and acts as frequency dependent delay which yields in temporally changes. GDD and GVD are associated with $\phi_2(\omega)L$. There is also a third order term known as third order dispersion (TOD) which adds a quadratic phase. [9] In general higher orders than TOD can be neglected which reformulates equation 6.4 to

$$E_{out}(\omega) = \sqrt{A_\omega e^{-\ln(2)(\frac{2(\omega-\omega_0)}{\Delta\omega})^2}}e^{-i(\varphi_{2,pulse}+\varphi_{2,mat})\frac{(\omega-\omega_0)^2}{2}} \tag{6.5}$$

To derive the pulse-duration inverse Fourier transformation has to be applied

$$E_{out}(t) = \sqrt{A'_t}e^{\frac{4\ln(2)t^2}{2(\Delta t^2+4i\ln(2)\varphi_2)}} \tag{6.6}$$

where φ_2 is denoted as GDD of the material and group delay of the pulse. To obtain the resulting pulse duration Δt_{out} the intensity $I_{out}(t)$ is required which can be derived by squaring the electric field $E_{out}(t)$ of equation 6.6

$$e^{-\ln(2)\left(\frac{2t}{\Delta t_{out}}\right)^2} = e^{\frac{4t^2\Delta t^2\ln(2)}{\Delta t^4+16\ln(2)^2\varphi_2^2}} \tag{6.7}$$

and solving for Δt_{out}

$$\Delta t_{out} = \frac{\sqrt{\Delta t^4 + 16\ln(2)^2\varphi_2^2}}{\Delta t} \tag{6.8}$$

GDD can now be expressed in terms of observables by solving equation 6.8 to φ_2 and replacing the transform limited pulse-duration with the spectral bandwidth which yields to

$$\varphi_2 = \frac{1}{4\ln(2)}\sqrt{\left(\frac{c_B\Delta t_{out}}{\Delta\nu}\right)^2 - \left(\frac{c_B}{\Delta\nu}\right)^4} \tag{6.9}$$

with $\Delta\nu = \frac{c\Delta\lambda}{\lambda^2}$. [9]

6.1.1. Dispersion compensation

This chapter refers to *Application Note 29: Prism Compressor for Ultrashort Laser Pulses* [9]. While propagating through dispersive materials a chirp is applied which can be compensated by negative GDD. This can be achieved with an arrangement of gratings or prisms. Therefore four prisms can be implemented while the first prism disperses the beam, the second collimates while third and fourth revert the effects of the first two prisms resulting in the same spatial output beam in comparison to the input beam. Normally the apex angle of prisms in prismcompressors is chosen to be the Brewster angle for a given wavelength to reduce reflection losses for p-polarized light. The resulting pathlength $P(\lambda)$ due to dispersion can be formulated as

$$P = 2l\cos(\beta) \tag{6.10}$$

where l is the distance between the apex angles of the prisms and β is the angle of dispersion. However, the introduced GDD can be described as

$$GDD_{prism} = \left(\frac{\lambda^3}{2\pi c^2}\right)\frac{d^2P(\lambda)}{d\lambda^2} \tag{6.11}$$

With the approach of Fork, Martinez, and Gordon [14] one can derive

$$GDD_{prism} = \frac{4l\lambda^3}{2\pi c^2}\left(\left(\frac{d^2n}{d\lambda^2} + \left(2n - \frac{1}{n^3}\right)\left(\frac{dn}{d\lambda}\right)^2\right)\sin(\beta) - 2\left(\frac{dn}{d\lambda}\right)^2\right) + \frac{8\lambda^3 D_{1/e^2}}{2\pi c^2}\frac{d^2n}{d\lambda^2} \tag{6.12}$$

where D_{1/e^2} is the beam diameter at $\frac{1}{e^2}$. [9] β can be approximated with

$$\beta \approx -2\frac{dn}{d\lambda}\Delta\lambda \tag{6.13}$$

The equation can be further simplified because β is relatively small and therefore equation 6.12 becomes

$$GDD_{prism} \approx \frac{\lambda^3}{2\pi c^2}\left[-4l\left(2\frac{dn}{d\lambda}\right)^2 + 4\frac{d^2n}{d\lambda^2}2D_{1/e^2}\right] \tag{6.14}$$

It can be seen that the first term is always negative and regards the separation distance l while the second term is always positive and treats the transversal position of the second prism and includes the beam-diameter. [9]

6.1.2. Experimental setup and measurements

In general a prismcompressor consists of four prisms but one can reduce the number of prisms to two if a mirror is used that tilts the beam under some degrees in vertical direction after the second prism and guides the beam backwards through both prisms. This has the advantage of easier alignment and less parts.

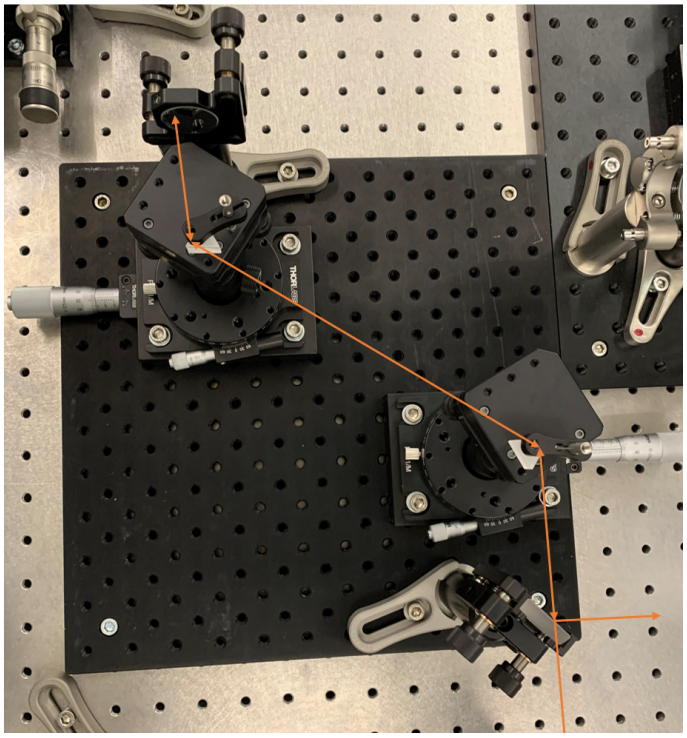

Figure 6.1.: Prismcompressor setup

Figure 6.1 shows the prismcompressor setup for pulse compression. Both prisms are made of SF10 and mounted on a translation- and rotation-stage. They are built for using them in Brewster configuration to reduce reflection losses. The beam enters the setup at the bottom right of the figure and passes two prisms. After that the ray is reflected by a mirror that additionally tilts the beam by some degrees in the vertical direction towards ground, re-enters both prisms and is picked up by a D-shaped mirror.

The experiment was performed in the following order

a First the GDD has to be evaluated that is responsible for enhancing the pulse duration and can be done by using equation 6.9 with a bandwidth of $\Delta\lambda = 100\,\text{nm}$ which yields to a GDD of $\varphi_2 = 3103\,\text{fs}^{-1}$.

b The transform limited pulse duration can be calculated with $\Delta t = \frac{c_B \lambda^2}{c\Delta\lambda}$ which gives $\Delta t = 8.8\,\text{fs}$. Therefore SF10 prisms can be used [9].

c Equation 6.14 has to be solved at $\lambda = 0.775\,\mu\text{m}$ with values for the first and second derivative derived from equation 5.2 and 5.3 which gives $\frac{dn}{d\lambda} = -0.0544\,\frac{1}{\mu\text{m}}$, $\frac{d^2n}{d\lambda^2} = 0.2028\,\frac{1}{\mu\text{m}^2}$ and a beam diameter of $D_{1/e^2} = 1.2 * 10^3\,\mu\text{m}$ in order to generate a positive GDD that is equal to $\varphi_2 = 3103\,\text{fs}^{-1}$ to find the required prism separation distance which can be accomplished at $l = 274.1\,\text{mm}$.

d Both prisms are adjusted to be in Brewster configuration which can be done by tilting the rotation stages to a point with minimum deviation of the exiting beam.

e The mirror is adjusted to tilt the reverted beam by a few degrees in vertical direction just enough to pick up the beam with the D-shaped mirror.

f For verification and fine adjustment the beam is in-coupled into the IAC after exiting the prismcompressor. Last corrections can be made with the translation stages because GDD can added or removed if the beam approaches to the tip of the prism or vice versa.

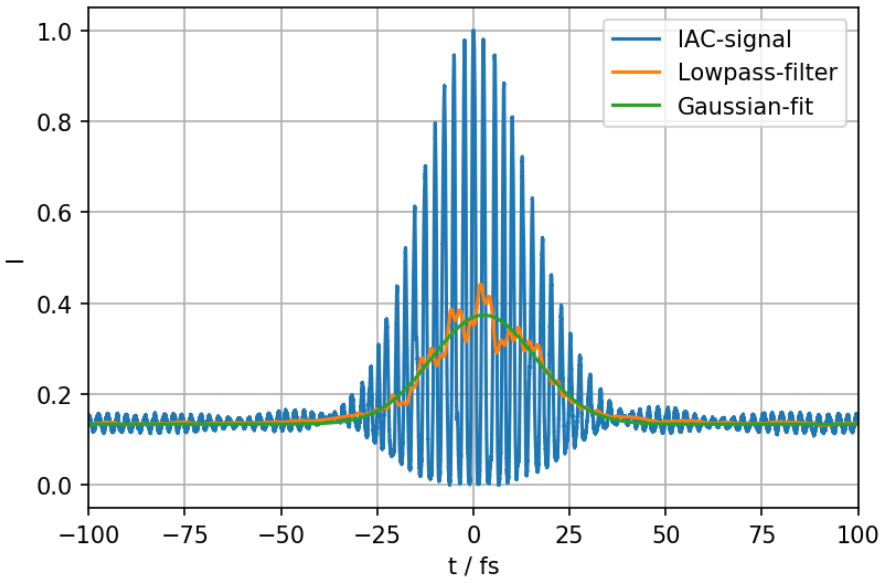

Figure 6.2.: Normalized interferometric autocorrelation of the compressed supercontinuum pulse with low-pass filtering to apply a Gaussian-fit.

Figure 6.2 shows the compressed pulse. To perform an analysis of the pulse-length a lowpass-filter is applied in the *Python*-code and then fitted with a Gauss-function. The pulse-duration can then be evaluated to be $\tau_{fwhm} = (23 \pm 1)$ fs.

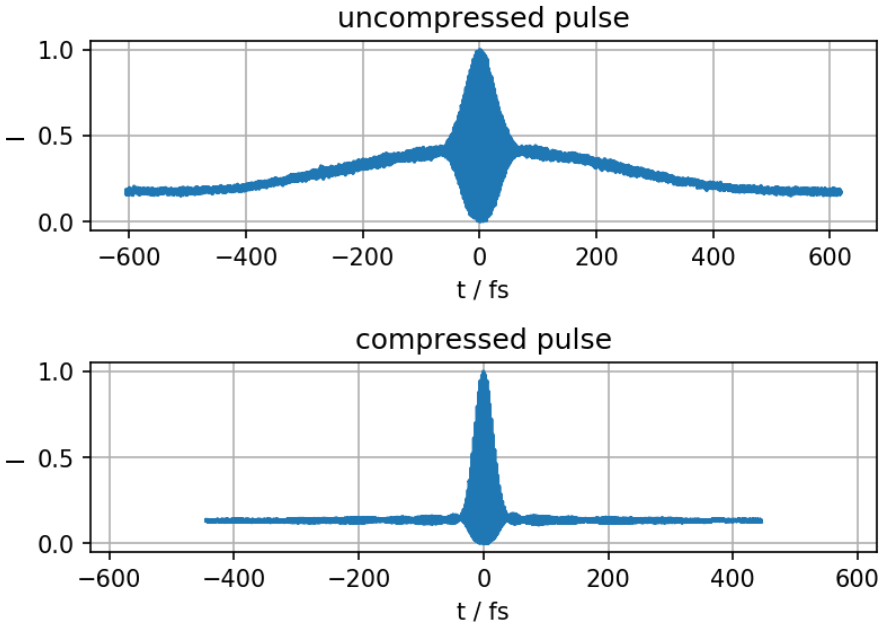

Figure 6.3.: Normalized interferometric autocorrelation of the compressed- and uncompressed pulse.

For better visualisation figure 6.3 shows the comparison of the compressed- and uncompressed-pulse. It can be seen that both graphs are symmetrical around 0 fs which indicates a good spacial overlap of the reference beam with its replica. For higher compression-rates GRISM- or chirped-mirror-compressors can be used in order to adjust second- and third-order dispersion individually. [6, 19]

7. Pulse-Chopping

7.1. Acousto-Optical Effect

Acoustic waves can be used to generate a grating due to a variation of the refractive index within a transparent medium. The grating structure which is produced by an electro-optic effect causes diffraction of optical waves inside the medium. [16]

The acousto-optic effect produces a change of the refractive index due to mechanical strain which is applied because of acoustic waves inside the medium. Due to the use of static waves the variation of the index of refraction remains periodic with a wavelength that is equal to the one of the acoustic wave. Mechanical strain therefore causes a variation in the refractive index which can manipulate the phase of the wave that is travelling through the medium. This effect is called photoelastic effect and is described with a fourth rank tensor that makes a relation between the strain tensor and the optical indicatrix. Induced mechanical strain results in periodic change of material density via the photoelastic effect along the acoustic wave. It was shown that the variation of the index of refraction Δn depends on the acoustic power P_a

$$\Delta n = \sqrt{n^2 p^2 10^7 \frac{P_a}{2\rho v_a^3 A}} \tag{7.1}$$

where n is the intrinsic refractive index, P_a is the acoustic power in Watts, p is the appropriate element of the photoelastic tensor, ρ is the material's density, v_a is the propagation velocity of the sound wave and A is the cross-section area of the travelling sound wave. [16]

In general crystalline solids are used as substrate for accousto-optical applications. Even if material and crystalline orientation is used properly the change in refractive index is in the order of $\Delta n = 10^{-4}$ even at high acoustic power densities of 100 $\frac{W}{cm^2}$. Small refractive index changes can lead to optical interactions that can accumulate constructively if phase matching is provided. [16]

Acousto-optical modulators (AOM) usually work with travelling acoustic waves that induce a grating structure that is in motion with the optical beam. This yields to a moving grating that causes a frequency shift by an amount equal to $\pm m f_0$ where m is the order and f_0 is the frequency of the acoustic wave. In most cases this shift is negligible. [16]

7.2. Experimental Data

There is a tightrope walk when choosing the proper AOM for applications with high switching rates. The possible picking rate is dependent on the traveling velocity of the crystal. Another circumstance that has to be taken into account is that small beam-sizes can be diffracted at higher picking rates while they are not allowed to be infinitely small due to diffraction efficiency decreases. In this experiment a AA.MT250-A0,12-800 from AA opto-electronic is used which is mounted on a translation stage and driven by a AA.PPKAc250-B-24 controller that is synchronized with the fiber-laser. The controller allows to adjust picking ratio, pulse delay, pulse width and power level of die radio-frequency (RF) generator that produces the acoustic wave.

The beam is focused according to VirtualLabs simulations with a 150 mm plano convex lens to receive a beam-diameter of 35 µm. The picking quality is evaluated with the ultrafast photodiode in order to find a proper pulse width of the RF-signal for efficiency optimisation and preventing to diffract parts of the temporal next laserpulse. After spatial optimisation of the AOM at a RF-pulsewidth of 12.5 ns an efficiency of 68 % was evaluated which matches with the expected value of 70 % according to the manufacturers datasheed at a pulse diameter of 35 µm. For collimation a 75.6 mm lens is used. The beam is then guided into a delay stage with a length of 30 cm and

a right-angle mirror for easier alignment. Temporal overlap between pump- and probe-beam is evaluated with the ultrafast photodiode.

8. Spectrometer

The aim was to find a suitable optical setup to build a spectrometer which is capable of covering the spectrum of the supercontinuum source in the range of $\approx (720 - 820)$ nm with a resolution of 1 nm. For analysing the supercontinuum-spectrum a grating-spectrometer should be implemented into the optical setup. Therefore the system was simulated with *LightTrans* to ensure a proper dimensioning of the components like lenses or grating.

8.1. Requirements

First of all, one needs to define the physical properties of the supercontinuum-source. However, the beam-diameter has a dimension of (2.1x2.1) μm^2 which results in a high divergence angle. Furthermore, as source of the simulation a Gaussian-beam was used and for efficiency considerations mostly three to ten wavelengths were considered to reduce the computational effort for field-tracing to a reasonable level.

8.2. Test-Setup with CMOS-Camera

First tests were performed with a THORLABS DCC1545M-GL CMOS camera which is used due to a chip size area (6.66x5.32) mm^2 that is comparable to the TOF camera (6.16x5.04) mm^2. For limiting the beam-diameter a 50 µm pinhole is used in front of the LA1304-B lens. The beam is focused with the LA1304-B plano-convex lens to illuminate the sample, collimated with LA1433-B, diffracted by a GR25-0608 blazed grating and then focused with a LA1608-B on the CMOS chip of the Thorlabs camera which is tilted by

Table 8.1.: Optical components used for spectrograph and simulation, f...focal length, $P-P$...Pixel-Pitch, ϕ...diameter

Component	Type-Lens	f / mm	Diameter
C151-TMD-B	Aspheric	2.0	3 mm
LA1304-B	Plano-Convex	40	1/2 ″
LA1608-B	Plano-Convex	75	1 ″
LA1433-B	Plano-Convex	150	1 ″
Component	Type	Groves/mm	Size / mm
GR25-0608	Blazed Grating	600	25x25x6
Component	Type-Camera	Size / pix	$P-P$ / µm
THORLABS DCC1545M-GL	CMOS	1280x1024	5.2

11° to compensate for chromatic aberration. The grating is mounted on a rotation- and tilting-stage to adjust for a horizontal beam path. The camera is additionally mounted on a translation stage to adjust the chip into the focal position.

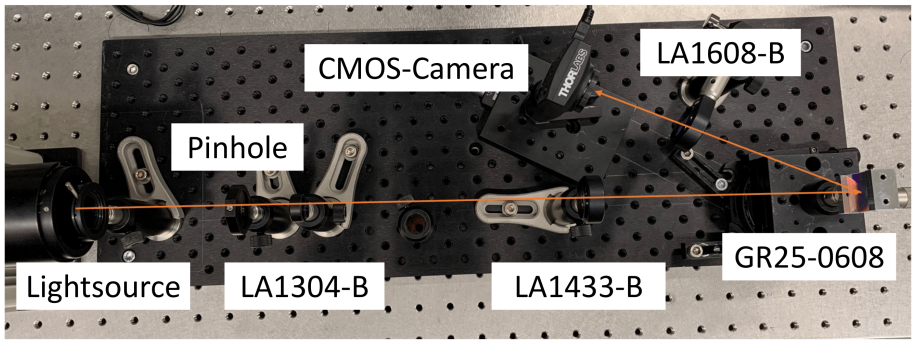

Figure 8.1.: Testsetup with THORLABS camera

Table 8.1 shows the components used for simulation and experiment with dimensions and properties.

Calibration with Xenon-Lamp

The first calibration is performed with a non fiber-coupled Xenon calibration-lamp because of its characteristical peaks in the infrared region. The spectrum is evaluated with the AVANTES spectrometer which can be seen in figure 8.2.

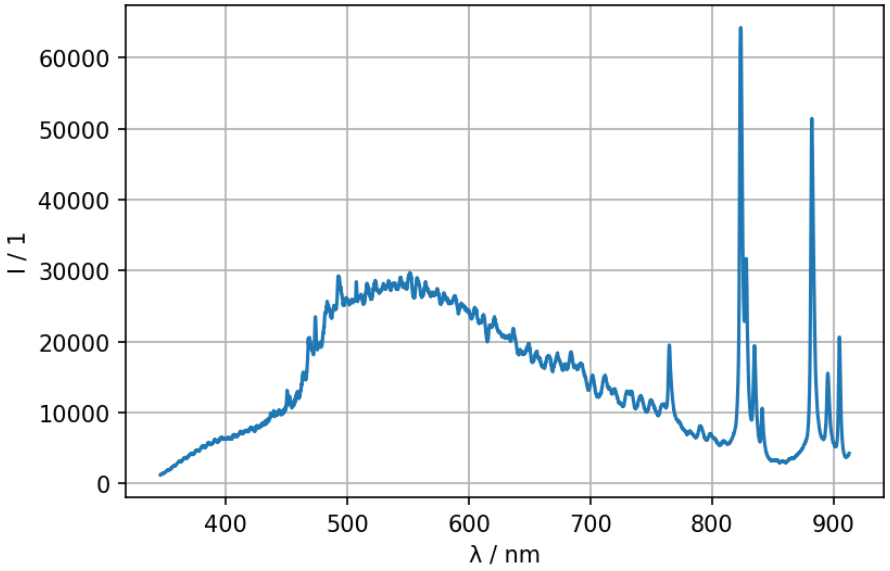

Figure 8.2.: Characteristical Xenon spectrum recorded with AVANTES spectrometer

It can be investigated that the characteristic peaks are between 800 nm and 950 nm so the horizontal axis is limited from 815 nm to 906 nm due to the chip-size area of the camera which can be seen in figure 8.3. The setup is therefore adjusted to cover a spectral range of 820 nm to 920 nm.

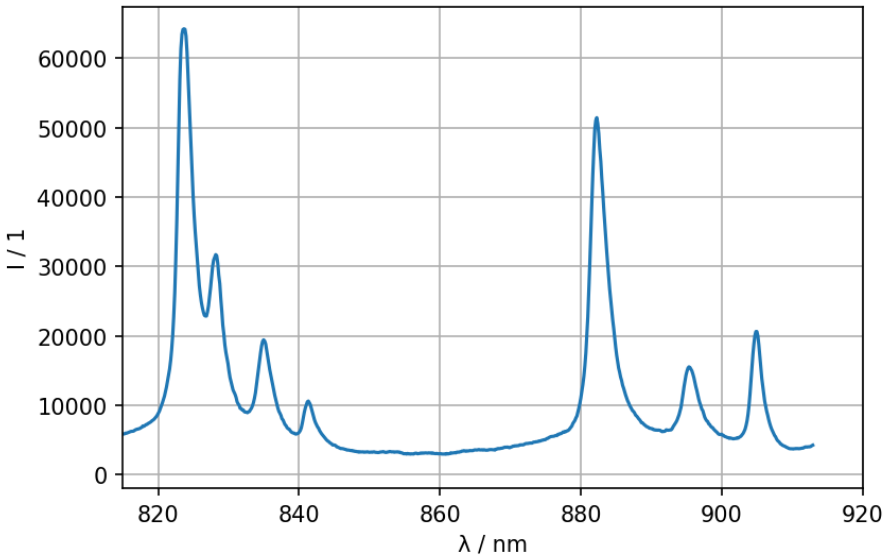

Figure 8.3.: Limited Xenon spectrum recorded with AVANTES spectrometer

After the first measurement with the AVANTES spectrometer the spectrum was measured with the test-setup from figure 8.1. The evaluation software of the THORLABS camera is able to provide a BITMAP file in which the intensity is stored as intensity/pixel. A *Python*-code is used to evaluate and plot the intensity of each pixel along the horizontal axis. The code can be investigated in appendix A.

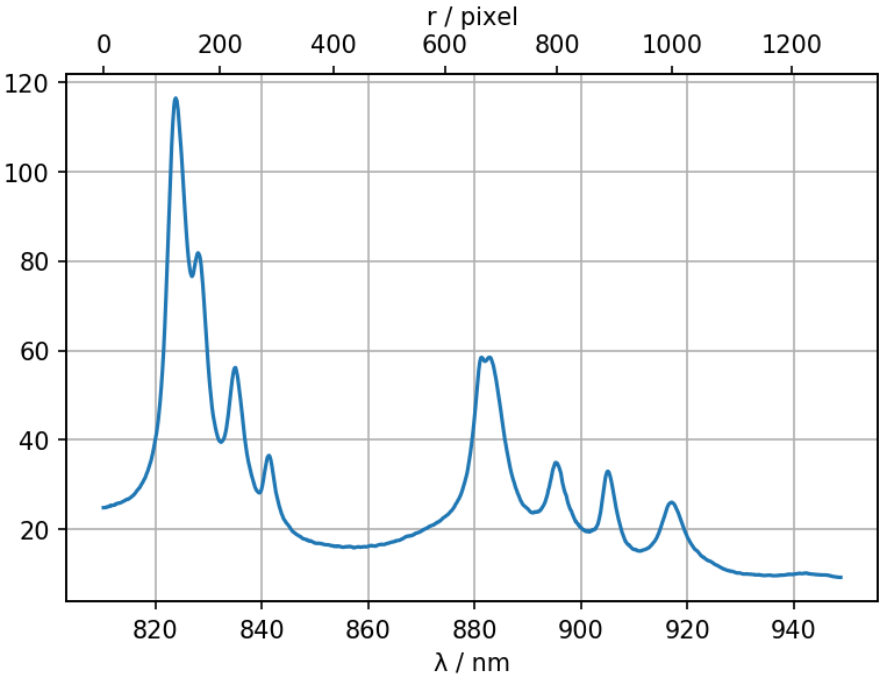

Figure 8.4.: Characteristic Xenon spectrum recorded with setup shown in figure 8.1 as function of the pixel number r in the upper abscissa and calibrated with a 3^{rd}-order polynomial in the lower abscissa as a function of λ

Figure 8.4 shows the measured spectrogram for a given spectral range. A calibration curve is established by fitting with a 3^{rd}-order polynomial which can be seen at the two different abscissa showing the uncalibrated and calibrated spectrum. The 3^{rd}-order polynomial looks as follows $\lambda = ar + br^2 + cr^3 + d$ where a, b and c are the fit parameters, r is the pixel-position and λ is the new wavelength. The fit-parameters are $a = (0.112 \pm 4 * 10^{-3}) \frac{\text{nm}}{\text{pix}}$, $b = (-1.35 * 10^{-5} \pm 8.4 * 10^{-6}) \frac{\text{nm}}{\text{pix}^2}$, $c = (8.3 * 10^{-9} \pm 5.4 * 10^{-9}) \frac{\text{nm}}{\text{pix}^3}$ and $d = (810.23 \pm 4.8 * 10^{-1})$ nm. The resolution of figure 8.4 can be determined at full width at half maximum and is $FWHM_{XEN} = (6.4 \pm 0.4)$ nm which is higher than the desired target of 1 nm.

Calibration with Fiber-Coupled Hg-Ar Lamp

For further tests a fiber-coupled Hg-Ar calibration lamp is used to perform a second calibration which is more accurate due to more peaks in the desired spectral range between 720 nm to 820 nm and an exact knowledge of peak-positions due to a datasheet. The setup remains the same as previously discussed in figure 8.1 except of the pinhole which is now 30 µm in diameter for a resolution advancement at the detector. The spectrum is evaluated with the *Python*-code from appendix A to plot the intensity of each pixel along the horizontal axis.

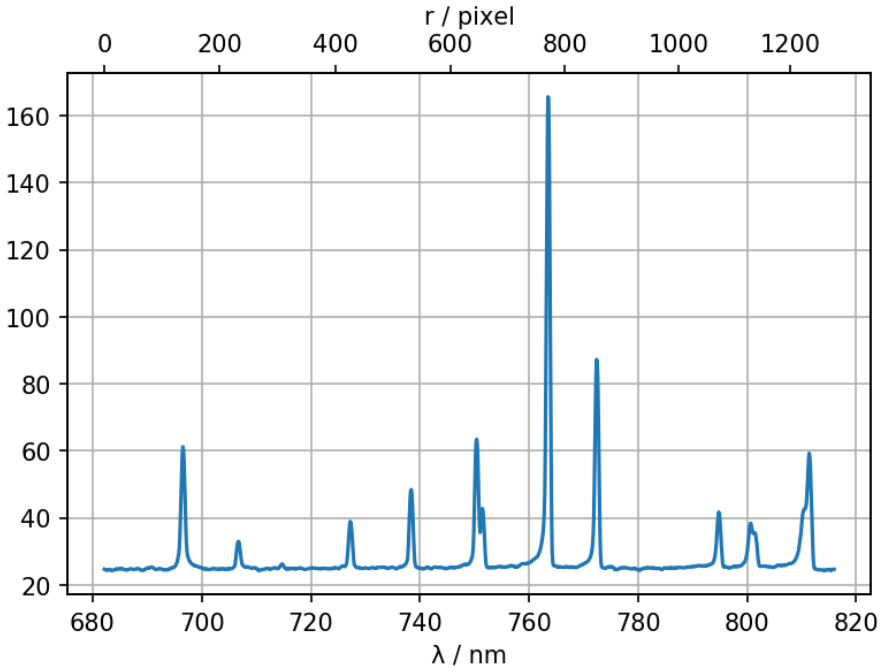

Figure 8.5.: Characteristic Hg-Ar spectrum recorded with setup shown in figure 8.1 as function of the pixel number r in the upper abscissa and calibrated with a 3rd-order polynomial in the lower abscissa as a function of λ

Figure 8.5 shows the calibrated spectrum as lower abscissa and uncalibrated spectrum as upper abscissa of the Hg-Ar source. Like in figure 8.4 the calibration fit consists of a 3rd-order polynomial $\lambda = ar + br^2 + cr^3 + d$ with

$a = (0.1057 \pm 5 * 10^{-4}) \frac{\text{nm}}{\text{pix}}$, $b = (7 * 10^{-7} \pm 9 * 10^{-7}) \frac{\text{nm}}{\text{pix}^2}$, $c = (-1.2 * 10^{-9} \pm 4 * 10^{-10}) \frac{\text{nm}}{\text{pix}^3}$ and $d = (682.16 \pm 9 * 10^{-2})\,\text{nm}$. The resolution of figure 8.5 can be evaluated at full width at half maximum and is $FWHM_{Hg-Ar} = (0.8 \pm 0.1)\,\text{nm}$ which is lower than the desired 1 nm resolution and the previous resolution of the Xenon-spectrum with $FWHM_{XEN} = (6.4 \pm 0.4)\,\text{nm}$. This can be explained with the usage of a smaller pinhole and an other type of lightsource that yields to very sharp peaks.

It can be seen that figure 8.5 captures more than 720 to 820 nm because according to tabular 8.3 100 nm in difference fill 5.179 mm of the chip horizontal length in comparison to the chip-size horizontal length of 6.656 mm.

8.3. Final Setup

The setup-components changed after the calibration with the Hg-Ar lamp. First of all it was recognized that after implementing the spectrometer into the setup it was not possible to collimate the beam properly due to long pathlenghts after the PCF with the C151-TMD-B because of its short focal length. Therefore the lens was substituted with a C390TME-B which has a slightly longer focal length f with 2.75 mm compared to 2.0 mm. Another aspect that led to a change of components is that pump- and probe-beam can not be focused sufficiently with a conventional plano-convex lens because of spherical-aberration which occurs due to different entering points of pump and probe which can be solved by using the achromatic lens AL2520-B. For collimating the beam a shorter focal length has to be chosen which leads to another LA1608-B.

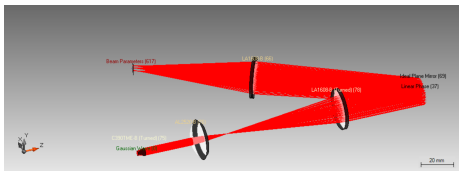

(a) Overwiev.

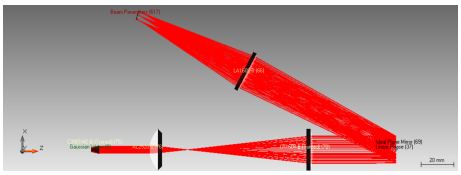

(b) Top view.

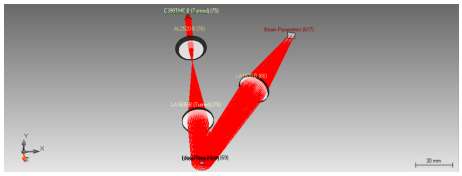

(c) Linear Phase.

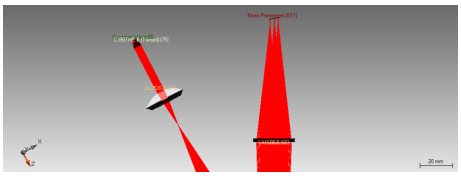

(d) Rotated Detector.

Figure 8.6.: Raytracing-simulation of optical components with *VirtualLabs Second Generation* in different views.

Figure 8.6 shows the optical setup visualised in different angles simulated with ray-tracing. The Gaussian-beam that is exiting the laser is collimated an then focused to expand the beam diameter. After expanding a grating is used to diffract the beam, here it is called ”Linear Phase” but more on this later. The beam is diffracted on a reflective blazed grating with 600 grooves/mm and a blaze angle of 13°.

8.3.1. Optical components

The setup consists of a C390TME-B that is collimating the beam after the PCF followed by an aspheric lens AL2520-B that is focusing the beam into the sample point, then the ray is collimated with a plano-convex lens LA1608-B onto the grid GR25-0608 and then focued with another LA1608-B onto the camera.

Table 8.2 shows the optical components used in the simulation and setup. In addition the camera is now mounted on a 3d-translation stage instead of a single axis stage. If a ”real” grating is considered with a grating period of 1/600 mm/groove this would yield to to 1.6̇ µm as grating constant d and would require two or more sampling points per period and additionally with

Table 8.2.: Optical components used for spectrograph and simulation, f...focal length, $P-P$...Pixel-Pitch, ϕ...diameter

Component	Type-Lens	f / m	ϕ
C390TME-B	Aspheric	3.1	5 mm
AL2520-B	Aspheric	20	1 ″
LA1608-B	Plano-Convex	75	1 ″
Component	Type	Groves/mm	Size / mm
GR25-0608	Blazed Grating	600	25x25x6
Component	Type-Camera	Size / pix	P-P / mAWD
ToF-Camera	CCD	352x288	17.5

a beam diameter of several mm the simulation would need an unreasonably high calculation effort. Therefore a ″Linear Phase″ is used to simulate an ideal diffraction grating which causes the wave to be deflected by a certain angle. Therefore, the required angle can be calculated with the grating-equation.

8.3.2. Simulation of the optical setup

To execute a fairly fast simulation 10 wavelengths are used. They were chosen in 10 nm steps to cover the whole spectrum from 720 nm to 820 nm. All simulations are restricted to first order diffraction. The ″Beam Parameters″ detector is calculating the different focal points for each wavelength on the screen which results because of the different beam-angles diffracted by the grating and their positions. The diffraction angles for the ″Linear Phase″ can be calculated via ″Parameter Coupling″. This tool allows to define dependencies of parameters with a programming toolbox. In addition to that the sensor is rotated at an angle of 13° clockwise to optimize for different focal points because of chromatic aberration caused by the lens system.

For further computation diffraction angles for the given wavelengths are required which can be calculated with

$$d \sin(\theta_m) = m\lambda \tag{8.1}$$

Because of the restriction to first order diffraction $m = 1$ one obtains

$$\theta_1 = \arcsin(\frac{\lambda}{d}) \tag{8.2}$$

with $d = 1.\dot{6} * 10^{-6}$ m.

Table 8.3.: Simulated beampositions with corresponding wavelength and diffraction angle, λ...wavelength, θ...diffraction-angle, x...position on the detector

λ / nm	θ / °	x / mm
820	29.472	2.599
810	29.078	2.068
800	28.685	1.541
790	28.294	1.016
780	27.905	0.493
770	27.516	-0.248
760	27.129	-0.540
750	26.744	-1.054
740	26.359	-1.566
730	25.976	-2.074
720	25.595	-2.580

Table 8.3 represents the simulated beampositions in one dimension with the corresponding wavelength and diffraction angle. It can be investigated that the beam position vary with different wavelengths according to the grating-equation 8.1.

The resolution of the spectrometer has to be determined. Therefore a simulation between 775 nm and 776 nm is performed to see if these wavelengths result in distinguishable points on the screen.

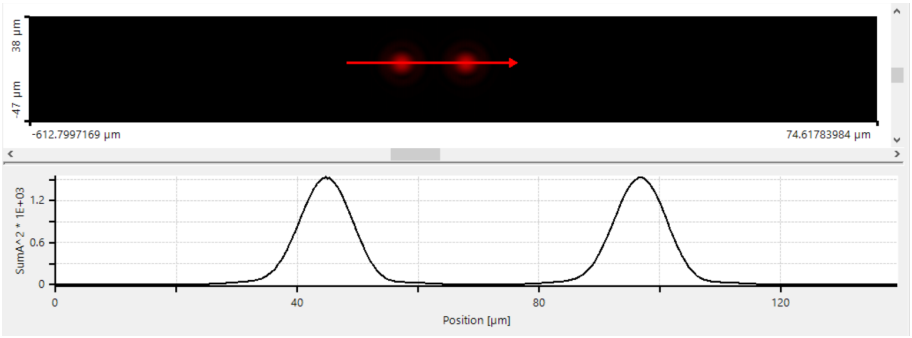

Figure 8.7.: Resolution of 1 nm, left dot corresponds to 775 nm-right dot to 776 nm.

Figure 8.7 shows two red points in the upper part that represent two wavelengths as 2d-intensity plot depending on position which corresponds to the visual representation of a human eye. The lower part of figure 8.7 shows the quantitative intensity distribution. However, it can be investigated that the points are distinguishable which leads to a resolution $< 1\,\text{nm}$. The setup is not calibrated now which will be done when the ToF-camera is implemented into the spectrograph. Therefore the resolution should remain approximately the same as in the previous measurement from figure 8.5 which yields to $FWHM_{Hg-Ar} = (0.8 \pm 0.1)\,\text{nm}$.

9. Evaluation of the Specimen Parameters

A specimen has to be selected that has a high molar attenuation coefficient in the wavelength range of the supercontinuum source which is $\Delta\lambda \approx (720 - 820)$nm. A suitable specimen is Indocyanine green which has a strong absorption around 782 nm.

9.1. Calculation of concentration

The sample has to be diluted to obtain a concentration c that results in $A = 50\,\%$ absorption which is a good reference value for spectroscopy. Due to the logarithmic behavior of the absorption one obtains

$$A = \log(\frac{I_0}{I}) = \log(2) = 0.301 \tag{9.1}$$

The law of Beer-Lambert relates the optical attenuation of light A propagating through a solution of a diluted species c with its molar attenuation coefficient ϵ with the pathlength l and can be described as

$$A = \epsilon c l \tag{9.2}$$

with ϵ / $\frac{\mathrm{L}}{\mathrm{molcm}}$, c / $\frac{\mathrm{mol}}{\mathrm{L}}$ and l / cm. [25] The molar attenuation coefficient at 782 nm is $\epsilon = 194 * 10^3 \frac{\mathrm{L}}{\mathrm{molcm}}$ according to Soper and Mattingly [28] and the pathlength $l = 0.01\,\mathrm{cm}$. Therefore one can obtain $c = \frac{A}{\epsilon l} = \frac{0.301}{194*10^3*0.01} = 1.55 * 10^{-4} \frac{\mathrm{mol}}{\mathrm{L}}$. Distilled water is a suitable substance for dilution.

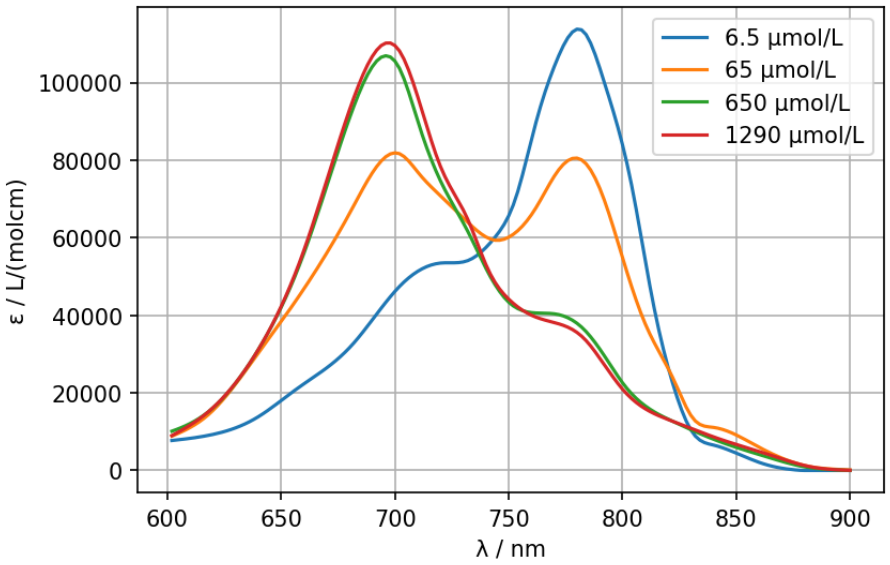

Figure 9.1.: Absorption spectra with variation of specimen concentration c diluted with distilled water. [21]

Landsman et al. [21] evaluated the attenuation coefficient ϵ dependent on the concentration of Indocyanine green in diluted water which can be seen in figure 9.1. It can observed that the absorption maximum strongly depends on the concentration which shifts to lower wavelengths with increasing amount of Indocyanine green. Low concentrations in the range of 6.5 $\frac{\mu mol}{L}$ like derived before do not shift the peak by a noticeable amount to lower wavelengths.

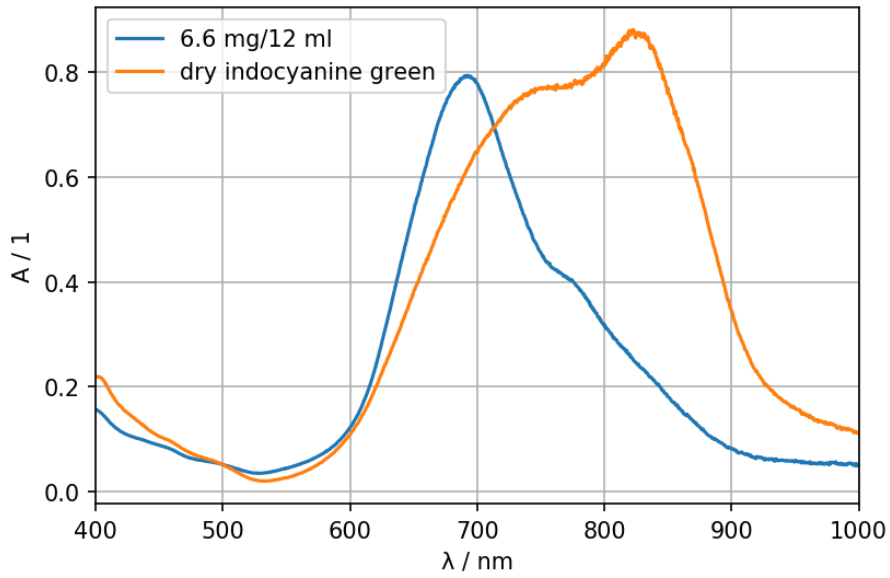

Figure 9.2.: Absorption spectra measured with the Agilent Spectrophotometer for Indocyanine green diluted with distilled water and solid powder.

The Indocyanine green powder is now diluted for the experiment at a higher concentration to be able to dilute the sample if required additionally. Figure 9.2 shows the absorption spectra measured with an Agilent Spectrophotometer for diluted- and solid-Indocyanine green at a concentration of $0.55\,\frac{\mathrm{g}}{\mathrm{L}}$ which corresponds to $7.09 * 10^{-4}\,\frac{\mathrm{mol}}{\mathrm{L}}$. It can be seen that the absorption-peak shifts to lower wavelengths but the absorption maximum is sufficient for the experiment.

A micro-cuvette is used that has a volume of $V = 26\,\mu\mathrm{L}$. Therefore the number of moles N that can fit inside the cuvette can be calculated with

$$N = cV = 7.09 * 10^{-4} * 26 * 10^{-6} = 1.85 * 10^{-8}\,\mathrm{mol} \tag{9.3}$$

Indocyanine green has a molar mass of $M = 775\,\frac{\mathrm{g}}{\mathrm{mol}}$ according to *PubChem-Indocyanine green* [22]. With the numer of moles N and the Avogadro-constant N_a one can calculate the number of molecules N_{cuv} inside the cuvette

$$N_{cuv} = N_a N = N_a * 1.85 * 10^{-8} = 1.11 * 10^{16} \text{ molecules} \tag{9.4}$$

9.1.1. Photons per Pulse and Excitation

The number of photons per laser pulse can be estimated by calculating the energy E_λ of a photon with a certain wavelength which is equal to

$$E_\lambda = \frac{hc}{\lambda} \tag{9.5}$$

with h as the Planck-constant, c is the speed of light and λ is the wavelength of the photon. We have an average power of $P_{av} = 13\,\text{mW}$ for the pump-beam in the sample-point at a wavelength of $\lambda = 775\,\text{nm}$. The energy of a photon with 775 nm can be calculated with equation 9.5 and yields to $E_{775} = 2.6 * 10^{-19}\,\text{J}$. To derive the number of photons the average laserpower P_{av} has to be devided by the single-photon energy E_{775} times the repetition rate of the pump-laser $R_r = 40 * 10^6\,\text{Hz}$. This leads to the number of photons

$$n_{ph} = \frac{P_{av}}{R_r E_{775}} = \frac{13 * 10^{-3}}{40 * 10^6 * 2.6 * 10^{-19}} = 1.27 * 10^9 \tag{9.6}$$

The beamprofiler and *Python*-code from appendix B is used to determine the beam-diameters of pump- and probe-beam in the sample point which can be seen in figure 9.4 for pump- and in figure 9.5 for probe-beam to determine the illuminated area of the specimen inside the cuvette and to verify if the probe-beam is larger than the pump-beam.

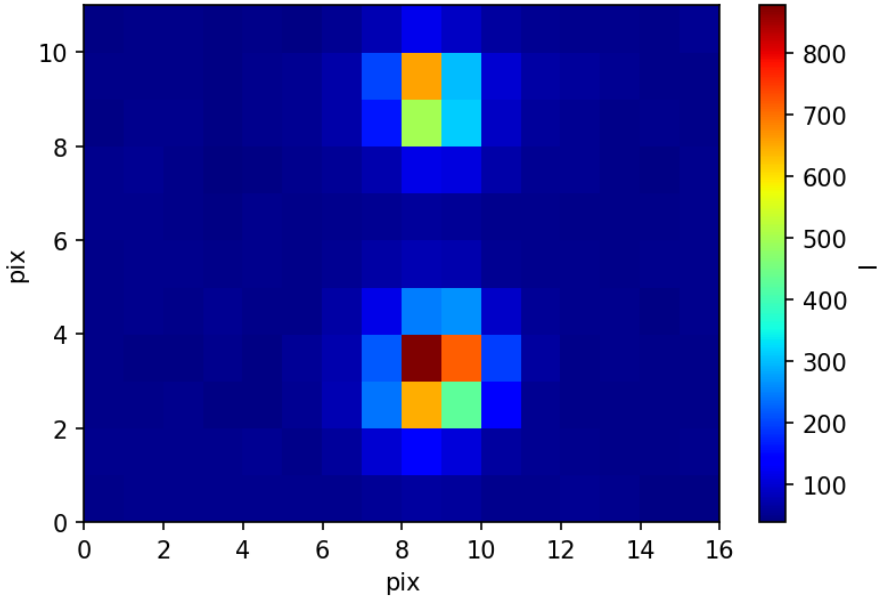

Figure 9.3.: Pump- and probe-beam separated vertically, top spot is pump- and bottom-spot is probe-beam.

It can be investigated that the beam-diameters in figure 9.3 in the focal point are too small to be detected with pixel-algorithms. Therefore, a sub-pixel algorithm is applied that fits the beam-intensity according to a Gaussfunction in vertical and horizontal direction and then evaluates the diameter at FWHM. The algorithm can be seen in appendix B. Both beams can be overlapped by adjusting the last mirror in the beam-path in front of the AL2520-B lens. This can be seen in figure 9.3.

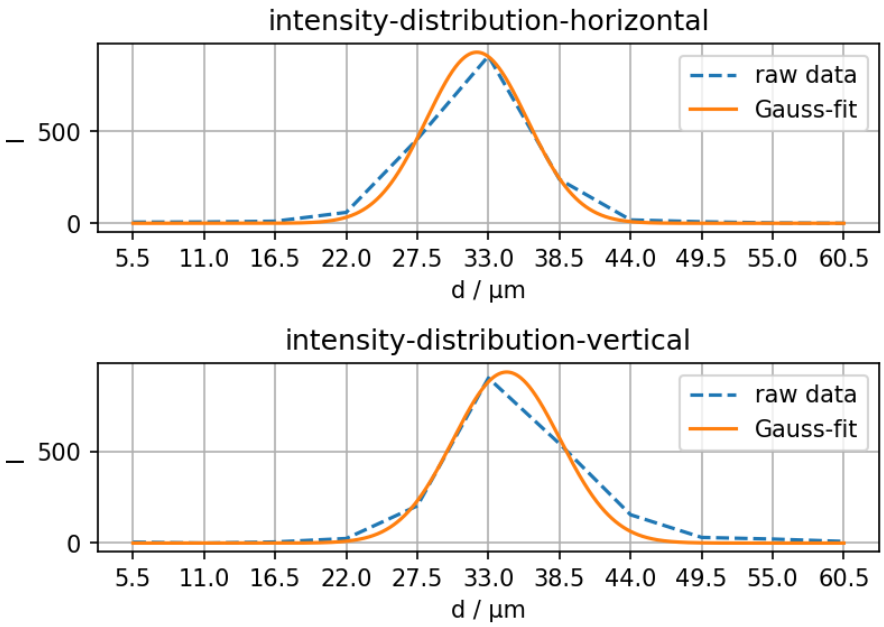

Figure 9.4.: Evaluation of the pump-beams spot-size with a sub-pixel algorithm from appendix B in vertical- and horizontal-direction.

The pump-beam-fits for horizontal- and vertical-diameter can be seen in figure 9.4. They are evaluated to be $\phi_{pump-vert} = (9.7 \pm 0.2)\,\mu m$ and $\phi_{pump-hor} = (9.2 \pm 0.1)\,\mu m$.

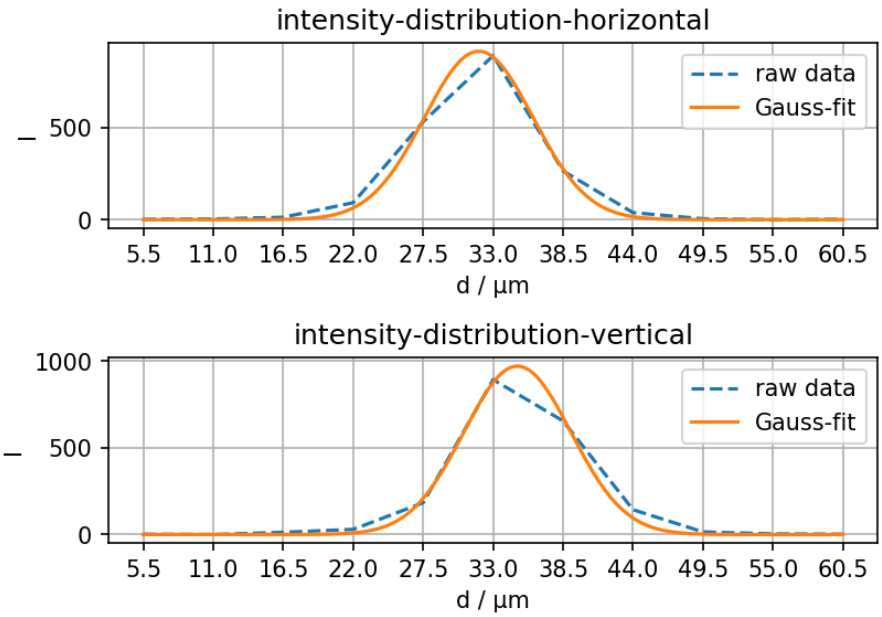

Figure 9.5.: Evaluation of the probe-beams spot-size with a sub-pixel algorithm from appendix B in vertical- and horizontal-direction.

The probe-beam-fits for horizontal- and vertical-diameter can be seen in figure 9.5. They are evaluated to be $\phi_{pump-vert} = (9.9 \pm 0.1)\,\mu m$ and $\phi_{pump-hor} = (10.1 \pm 0.1)\,\mu m$. It can be seen that the pump-beam is smaller than the probe-beam which is required because the probe-beam should cover the entire area of the pump-beam to gather all information from the excitation. The spotsize of the pump-beam in the sample-point is therefore $\phi_{probe-h,v} \approx 9.45\,\mu m$ in diameter if the average is calculated.

Now the volume of the illuminated cuvette V_{ill} can be calculated with

$$V_{ill} = \phi^2_{probe-h,v} * \frac{\pi}{4} * d_{cuv} = 7.01 * 10^{-9}\,\mu L \tag{9.7}$$

where d_{cuv} is the thickness of the cuvette which is equal to 0.1 mm.

To derive the number of particles that are inside of the cuvette in the desired volume one has to multiply the illuminated volume with the number of particles per volume in the cuvette which yields to $n_{pv} = 2.99 * 10^6$ particles.

To obtain the number of excited molecules the absorption cross-section of Indocyanine green has to be evaluated wich was done by Yaqoob et al. [34] in water to be $\sigma = 2.08 * 10^{-16}\,\mathrm{cm}^2$. The probability of the photons to excite molecules can then be calculated with

$$p_{ex} = \frac{n_{pv}\sigma}{A_{ill}} \tag{9.8}$$

where A_{ill} is the illuminated area on the cuvette which gives $p_{ex} = 8.87 * 10^{-4}$. To derive the number of excited molecules the probability for excitation p_{ex} has to be multiplied with the number of photons from the laserbeam n_{ph} which yields to $1.12 * 10^6$ excited molecules.

10. Pump-Probe Experiment

This chapter describes the final measurement of the pump- and probe-experiment of Indocyanine green with the ultrafast photodiode DET210 and a lock-in amplifier. The setup remains the same like described in chapter 8.3 but instead of the camera the ultrafast photodiode is inserted. Therefore only single-wavelength measurements are possible.

The DET210 is connected to the lock-in amplifier and the signal goes further from the amplifier to the picoscope. The time-constant τ is set to 6 dB with a sensitivity of 20 times in the µV region. The AOM was adjusted to have minimal side-bands of the next pulses. The best RF-length is determined to be 12.5 ns to minimize the sidebands from the laser. Figure 10.1 shows the trigger-signal from the laser-source which acts as input-signal to the AOM-controller. The signal from the RF-generator is the 40 MHz output from the AOM which enables pulse-picking. The last plot on the bottom shows the picked laserpulses, if one has a close look small sidebands can be seen but they are sufficient for the experiment.

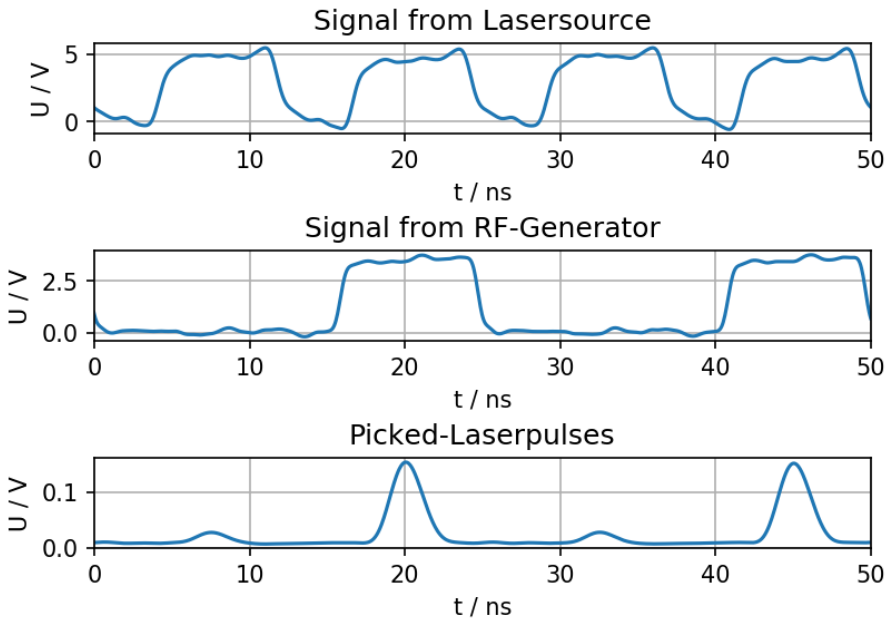

Figure 10.1.: Measurement of the Laser-Trigger-Signal, RF-Signal to AOM and the Picked-Laserpulses with the Teledyne Lecroy Oscilloscope.

In figure 10.2 one can investigate the measured intensity difference of probe-with pump- and without pump-pulse. The repetition time of the probe pulse is $t_{rep} = 12.5\,\text{ns}$. For explanation purposes t_{pp} is the time between pump- and probe-signal which is varied with the translation stage. If the pump- is shortly before the probe-pulse, which means $t_{pp} > 0$, then the effect of the pump- on the probe-pulse after the delay of t_{pp} is captured. For $t_{pp} < 0$, which means that the pump-pulse is shortly after the probe-pulse, the current pump- should have no effect on the probe-pulse but a signal from the previous pump-pulse is observed which means that the sample has not enough time to relax to ground state for $< t_{rep}$.

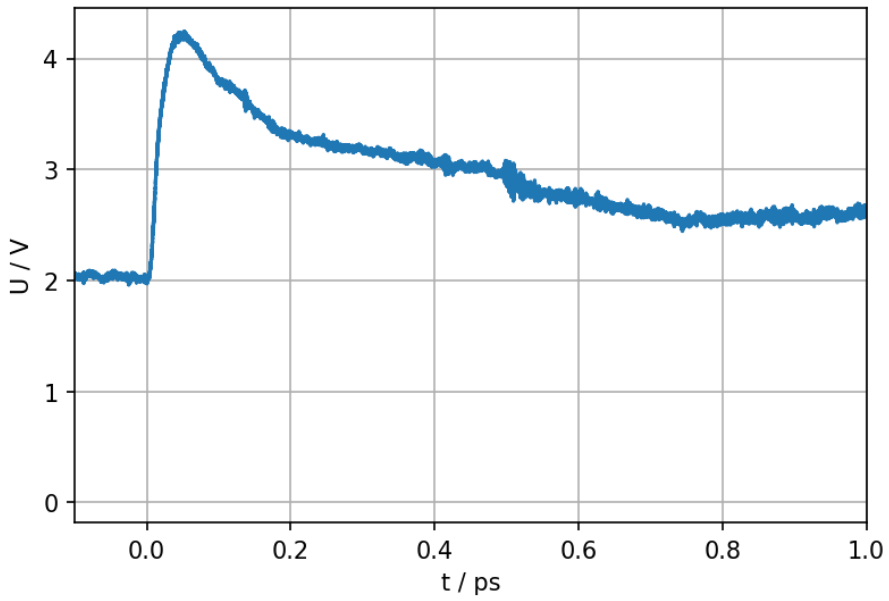

Figure 10.2.: Pump-Probe signal derived from Cyanine Green at a wavelength of ≈ 800 nm with a 40 MHz repetition-rate and 13 mW average-power pump-pulse operating at 775 nm, 80 MHz repetition-rate and 67 mW probe-pulse operating at (720-820) nm, measured signal with DET210 ultrafast photodiode and amplified with the lock-in amplifier.

With figure 10.2 and a separate measurement of the photodiode voltage with the digital oscilloscope from Pico Technology one can calculate the relative signal change that results from excitation of the sample. On the output side of the lock-in amplifier one obtains $V_o = 10\,\mathrm{V}$ for the measurement range and $V_{sens} = 20\,\mu\mathrm{V}$ for the sensitivity setting of the photodiode on the lock-in amplifier. With the maximum of figure 10.2 which is $V_L = (4.2 \pm 0.1)\,\mathrm{V}$ one can calculate the signal change of the pump-beam to be $\frac{V_L}{V_o} V_{sens} = (8.4 \pm 0.1)\,\mu\mathrm{V}$. The signal of the diode is $V_d = (6.7 \pm 0.1)\,\mathrm{V}$ which then causes a signal change of

$$\frac{\Delta I}{I} = \frac{V_L V_{sens}}{V_o V_d} = (1.25 \pm 0.05) * 10^{-3} \tag{10.1}$$

With 10.1 the change in optical density can be calculated with

$$\Delta OD = \log(1 + \frac{\Delta I}{I}) = (5.44 \pm 0.02) * 10^{-4} \tag{10.2}$$

which means that the optical density of the sample changes by the calculated amount when the pump-pulse excites the system. [17]

Appendix

Appendix A.

Python-Code for BITMAP Evaluation

```
from PIL import Image
import numpy as np
import matplotlib.pyplot as plt
from scipy.signal import savgol_filter
from scipy.optimize import curve_fit

# Import of the BITMAP-Picture

path = r'PATH:\FILE.bmp'

img = Image.open(path)
img_arr = np.array(img)
img_arr = img_arr[:,:,0]

# Mean of n values around the maximum (only even values)
n = 6

# Searching inside the boarders of +- m pixels around the horizontal
# axis
m = 10


img_arr_max = np.where(np.max(img_arr) == img_arr)
```

```
img_arr = img_arr[(img_arr_max[0][0]-m):(img_arr_max[0][0]+m),:]
shape = np.array(np.shape(img_arr))
x_pix = np.linspace(0,shape[1]-1,shape[1])

# Finding the intensity maxima along the y-axis
intens = np.zeros((shape))
intens_mean = np.zeros((shape[1],1))
intens_mean_n = np.zeros((n+1,shape[1]))
img_arr_index = np.zeros((n+1,shape[1]))
img_arr_mean = np.zeros((shape[1],1))

# Loop over all horizontal pixels
for x in range(0,shape[1]):
    # Finding the maxima
    max_intens = np.where(np.max(img_arr[:,x]) == img_arr[:,x])

    # Storing the maxima into the zero matrix intens
    for y in range(0,np.size(max_intens)):
        intens[y,x] = max_intens[0][y]

    # Finding the mid maximum value
    intens_mean[x] = np.round(np.mean(
            intens[0:np.size(max_intens),x]))

    # n values in vertical position from the maximum value
    # If the maximum is at the outer boarder, the n values
    # above the maxima were chosen
    if (intens_mean[x]+n/2) >= (2*m-1):
        for u in range(0,np.size(np.linspace(
                intens_mean[x],intens_mean[x]-n,n+1))): \
            intens_mean_n[u,x] = np.linspace( \
                    intens_mean[x],intens_mean[x]-n,n+1)[u]
            img_arr_index[u,x] = img_arr[ \
                    intens_mean_n.astype(int)[u,x],x]
    else:
        for u in range(0,np.size(np.linspace(intens_mean[x]- \
                                             n/2,intens_mean[x]+ \
```

```
                                                    n/2,n+1))):
                intens_mean_n[u,x] = np.linspace(intens_mean[x]- \
                                n/2,intens_mean[x]+n/2,n+1)[u]
                img_arr_index[u,x] = img_arr[ \
                        intens_mean_n.astype(int)[u,x],x]

        # Calculating the mean value of n+1 pixels in
        # vertical position
        img_arr_mean[x] = np.mean(img_arr_index[:,x])
        img_arr_mean = np.reshape(img_arr_mean, (np.product(
                img_arr_mean.shape),)) # ND- to 1D-array

# Smoothing the data according to a Savgol-filter
img_arr_SG = savgol_filter(img_arr_mean,  \
                           window_length = 7, polyorder = 1)

#Find the maxima of img_arr_SG and the according wavelength
charact_max_intens = np.array([1, 2, 3, 4, 5, 6])
charact_max_lamb = np.array([1, 2, 3, 4, 5, 6])

#Find a fit-function
def scale(x_pix,a_fit,b_fit,c_fit,d_fit):
    return a_fit*x_pix+b_fit*x_pix**2+c_fit*x_pix**3+d_fit

param, param_cov = curve_fit(scale, charact_max_lamb, \
                             charact_max_intens,maxfev=10000)
x_pix_scale = scale(x_pix,param[0],param[1],param[2],param[3])

# Plot of the results
plt.figure(dpi = 150)
plt.plot(x_pix_scale,img_arr_SG)
plt.grid()
plt.xlabel('wavelength / nm')
plt.ylabel('I / 1')
```

Appendix B.

Python-Code for Beam-Diameter Evaluation with Sub-Pixel Algorithm

```
# Beam-Diameters of Pump- and Probe-Beam
# The pixel-size is (5.5 x 5.5) micrometers

import numpy as np
import matplotlib.pyplot as plt
import pandas as pd
from scipy.optimize import curve_fit

probe_file = r'Path:\Probe_Beam.csv'
pump_file =  r'Path:\Pump_Beam.csv'
pump_probe_file =  r'Path:\pump_probe_beams.csv'

probe_mat = np.rot90(np.asarray(pd.read_csv(probe_file)))
pump_mat = np.rot90(np.asarray(pd.read_csv(pump_file)))
pump_probe_mat = np.rot90(np.asarray(pd.read_csv(pump_probe_file)))

probe_int_max = np.where(probe_mat == np.max(probe_mat))
pump_int_max = np.where(pump_mat == np.max(pump_mat))
pump_probe_int_max = np.where(pump_probe_mat ==
                              np.max(pump_probe_mat))
```

```
def gauss(x,a,xo,sigma,offset):
    return a*np.exp(-(x-xo)**2/(2*sigma**2))-offset

def find_nearest(array, value):
    array = np.asarray(array)
    idx = (np.abs(array - value)).argmin()
    return array[idx]

def FWHM(gauss_fit,gauss_vec):
    half = (np.max(gauss_fit) - np.min(gauss_fit))/2
    nearest_1 = find_nearest(gauss_fit[0:np.int(np.round(
            np.size(gauss_fit)/2))],half)
    nearest_2 = find_nearest(gauss_fit[np.int(
            np.round(np.size(gauss_fit)/2)):-1],half)
    FWHM = [np.where(gauss_fit == nearest_1),
            np.where(gauss_fit == nearest_2)]
    return np.asscalar(np.abs((gauss_vec[FWHM[0]] -
                               gauss_vec[FWHM[1]])))


n = 5 #n-Pixels around the maximum
pix_size = 5.5
pix_vec = pix_size*np.linspace(1,2*n+1,2*n+1)
pix_gauss = np.linspace(pix_size,np.max(pix_vec),1000)

#Probe-beam
probe_vec_hor = np.int64(np.linspace(np.asscalar( \
        probe_int_max[0])- \
        n,np.asscalar(probe_int_max[0])+n,
                      2*n+1))
probe_vec_vert = np.int64(np.linspace(np.asscalar( \
        probe_int_max[1])- \
        n,np.asscalar(probe_int_max[1])+n,2*n+1))

probe_int_hor = probe_mat[probe_vec_hor,probe_int_max[1]] - \
                np.min(probe_mat[probe_vec_hor,probe_int_max[1]])
probe_int_vert = probe_mat[probe_int_max[0],probe_vec_vert] - \
```

```
                    np.min(probe_mat[probe_int_max[0],probe_vec_vert])

param_probe_vert, probe_cov_vert = curve_fit(gauss,pix_vec, \
                                             probe_int_vert,maxfev=10000)
gauss_probe_vert = gauss(pix_gauss,*param_probe_vert)

param_probe_hor, probe_cov_hor = curve_fit(gauss,pix_vec, \
                                           probe_int_hor,maxfev=10000)
gauss_probe_hor = gauss(pix_gauss,*param_probe_hor)
FWHM_probe_hor = FWHM(gauss_probe_hor,pix_gauss)
FWHM_probe_vert = FWHM(gauss_probe_vert,pix_gauss)
print('FWHM_probe_horizontal_=', FWHM_probe_hor ,'micrometer')
print('FWHM_probe_vertical_=', FWHM_probe_vert ,'micrometer')

#Plot for Probe-beam
m = 5 #only use odd numbers

plt.figure(dpi=150)
cbar = plt.pcolormesh(probe_mat[np.asscalar(probe_int_max[0])- \
                                m:np.asscalar(probe_int_max[0])+m \
                               ,np.asscalar(probe_int_max[1])- \
                               m:np.asscalar(probe_int_max[1])+m], \
                               cmap = 'jet')
plt.colorbar(cbar,label='I')
plt.yticks(np.linspace(2,2*m,m))
plt.xlabel('pix')
plt.ylabel('pix')

fig1,(ax1,ax2) = plt.subplots(2,dpi=150)
plt.subplots_adjust(wspace=1, hspace=0.7)
ax1.plot(pix_vec,probe_int_hor,'--',label = 'raw_data')
ax1.plot(pix_gauss,gauss_probe_hor,label = 'Gauss-fit')
ax1.set_title('intensity-distribution-horizontal')
ax1.legend(loc='upper_right')
ax1.grid('on')
ax1.set_xticks(pix_vec)
ax1.set_xlabel('d_/_micrometer')
```

```
ax1.set_ylabel('I')
ax2.plot(pix_vec,probe_int_vert,'--',label = 'raw data')
ax2.plot(pix_gauss,gauss_probe_vert,label = 'Gauss-fit')
ax2.set_title('intensity-distribution-vertical')
ax2.legend(loc='upper right')
ax2.grid('on')
ax2.set_xticks(pix_vec)
ax2.set_xlabel('d / micrometer')
ax2.set_ylabel('I')

#Pump-beam
pump_vec_hor = np.int64(np.linspace(np.asscalar(
               pump_int_max[0])- \
               n,np.asscalar(pump_int_max[0])+n,2*n+1))
pump_vec_vert = np.int64(np.linspace(np.asscalar( \
               pump_int_max[1])- \
               n,np.asscalar(pump_int_max[1])+n,2*n+1))
pump_int_hor = pump_mat[pump_vec_hor,pump_int_max[1]] - \
                np.min(pump_mat[pump_vec_hor,pump_int_max[1]])
pump_int_vert = pump_mat[pump_int_max[0],pump_vec_vert] - \
                np.min(pump_mat[pump_int_max[0],pump_vec_vert])
param_pump_hor, pump_cov_hor = curve_fit(gauss, pix_vec, \
                                  pump_int_hor,maxfev=10000)
param_pump_vert, pump_cov_vert = curve_fit(gauss, pix_vec, \
                                      pump_int_vert,maxfev=10000)

gauss_pump_hor = gauss(pix_gauss,*param_pump_hor)
gauss_pump_vert = gauss(pix_gauss,*param_pump_vert)
FWHM_pump_hor = FWHM(gauss_pump_hor,pix_gauss)
FWHM_pump_vert = FWHM(gauss_pump_vert,pix_gauss)
print('FWHM_pump_horizontal =', FWHM_pump_hor ,'micrometer')
print('FWHM_pump_vertical =', FWHM_pump_vert ,'micrometer')

#Plot for Pump-beam
k = 5 #only use odd numbers
plt.figure(dpi=150)
cbar = plt.pcolormesh(pump_mat[np.asscalar(pump_int_max[0])- \
```

```
                                    k:np.asscalar(pump_int_max[0])+k \
                                ,np.asscalar(pump_int_max[1])-k: \
                                    np.asscalar( \
                                        pump_int_max[1])+k],cmap = 'jet')
plt.colorbar(cbar,label='I')
plt.yticks(np.linspace(2,2*k,k))
plt.xlabel('pix')
plt.ylabel('pix')


fig2,(ax3,ax4) = plt.subplots(2,dpi=150)
ax3.plot(pix_vec,pump_int_hor,'--',label = 'raw data')
ax3.plot(pix_gauss,gauss_pump_hor,label = 'Gauss-fit')
ax3.set_title('intensity-distribution-horizontal')
ax3.legend(loc='upper right')
ax3.grid('on')
ax3.set_xticks(pix_vec)
ax3.set_xlabel('d / micrometer')
ax3.set_ylabel('I')
plt.subplots_adjust(wspace=1, hspace=0.7)
ax4.plot(pix_vec,pump_int_vert,'--',label = 'raw data')
ax4.plot(pix_gauss,gauss_pump_vert,label = 'Gauss-fit')
ax4.set_title('intensity-distribution-vertical')
ax4.legend(loc='upper right')
ax4.grid('on')
ax4.set_xticks(pix_vec)
ax4.set_xlabel('d / micrometer')
ax4.set_ylabel('I')

#Pump-Probe-beam
#Plot for pump-probe-beam
l = 8
i = 3
plt.figure(dpi=150)
plt.pcolormesh(pump_probe_mat[np.asscalar(probe_int_max[0])-i:\
    np.asscalar(probe_int_max[0])+l \
                                ,np.asscalar(probe_int_max[1])-l: \
```

```
                                    np.asscalar(probe_int_max[1])+1], \
                                cmap = 'jet')
plt.colorbar(label="I")
plt.xlabel('pix')
plt.ylabel('pix')
```

Bibliography

[1] Esben Ravn Andresen. "Fiber-based Implementations of Coherent anti-Stokes Raman Scattering Microspectroscopy and Microscopy." PhD thesis. Department of Physics and Astronomy, University of Aarhus, Denmark, 2007 (cit. on pp. 10, 12–14).

[2] Matthieu Baudelet. *Laser Spectroscopy for Sensing: Fundamentals, Techniques and Applications*. Elsevier, 2014, pp. 11–17 (cit. on p. 1).

[3] BlazePhotonics. *Highly nonlinear PCF - Datasheet BlazePhotonics*. Bath, Bath and North East Somerset, United Kingdom: blazephotonics, June 2004, p. 1. 4 pp. (cit. on p. 16).

[4] Wolfgang Bludau. *Lichtwellenleiter in Sensorik und optischer Nachrichtentechnik*. Springer-Verlag, 2013, p. 297 (cit. on pp. 27, 28).

[5] Robert W Boyd. *Nonlinear optics*. Academic press, 2019, p. 1 (cit. on p. 2).

[6] Vikrant Chauhan et al. "Single-diffraction-grating and grism pulse compressors." In: *J. Opt. Soc. Am. B* 27.4 (Apr. 2010), pp. 619–624. DOI: 10.1364/JOSAB.27.000619. URL: http://josab.osa.org/abstract.cfm?URI=josab-27-4-619 (cit. on p. 41).

[7] Ji-Xin Cheng and Xiaoliang Sunney Xie. *Coherent Raman scattering microscopy*. CRC press, 2016, pp. 4–6 (cit. on pp. 10, 11, 13).

[8] Majed Chergui and John Thomas. "From structure to structural dynamics: Ahmed Zewail's legacy." In: *Structural Dynamics* 4 (July 2017), pp. 2–4. DOI: 10.1063/1.4998243 (cit. on pp. 1, 2, 4).

[9] Newport Corporation. *Application Note 29: Prism Compressor for Ultrashort Laser Pulses*. Spectra-Physics. 1791 Deere Avanue Irvine, CA 92606: Newport Corporation, 2020, pp. 1–12. 12 pp. URL: https://www.newport.com/medias/sys_master/images/images/h25/h7f/8797242818590/Prism-Compressor-for-Ultrashort-Laser-Pulses-App-Note-29.pdf (visited on 2020) (cit. on pp. 34–37, 39).

[10] Jean-Claude Diels and Wolfgang Rudolph, eds. *Ultrashort Laser Pulse Phenomena (Second Edition)*. Burlington: Academic Press, 2006, pp. 491–652 (cit. on pp. 4, 13, 27, 29).

[11] John M Dudley, Goëry Genty, and Stéphane Coen. "Supercontinuum generation in photonic crystal fiber." In: *Reviews of modern physics* 78.4 (2006), pp. 1135–1140 (cit. on pp. 8, 9).

[12] Tijmen G Euser, Philip J Harding, and Willem L Vos. "Broadband sensitive pump-probe setup for ultrafast optical switching of photonic nanostructures and semiconductors." In: *Review of scientific instruments* 80.7 (2009), p. 073104 (cit. on p. 18).

[13] M. G. Evans and M. Polanyi. "Some applications of the transition state method to the calculation of reaction velocities especially in solution." In: *Trans. Faraday Soc.* 31 (0 1935), pp. 875–894. DOI: 10.1039/TF9353100875 (cit. on p. 1).

[14] R. L. Fork, O. E. Martinez, and J. P. Gordon. "Negative dispersion using pairs of prisms." In: *Opt. Lett.* 9.5 (May 1984), pp. 150–152. DOI: 10.1364/OL.9.000150. URL: http://ol.osa.org/abstract.cfm?URI=ol-9-5-150 (cit. on p. 37).

[15] Jeffrey Guttman. "Mode-Field Diameter and "Spot Size" Measurements of Lensed and Tapered Specialty Fibers." In: (Jan. 2002) (cit. on p. 17).

[16] Robert G. Hunsperger. "Acousto-Optic Modulators." In: *Integrated Optics: Theory and Technology*. Berlin, Heidelberg: Springer Berlin Heidelberg, 2002, pp. 175–191. ISBN: 978-3-540-38843-2. DOI: 10.1007/978-3-540-38843-2_10. URL: https://doi.org/10.1007/978-3-540-38843-2_10 (cit. on pp. 42, 43).

[17] James Johnston, Terri L Fauber, et al. *Essentials of radiographic physics and imaging*. Elsevier Health Sciences, 2015 (cit. on p. 67).

[18] Florian Kanal et al. "100-kHz shot-to-shot broadband data acquisition for high-repetition-rate pump–probe spectroscopy." In: *Opt. Express* 22.14 (July 2014), pp. 16965–16975. DOI: 10.1364/OE.22.016965. URL: http://www.opticsexpress.org/abstract.cfm?URI=oe-22-14-16965 (cit. on p. 2).

[19] S. Kane and J. Squier. "Grism-pair stretcher–compressor system for simultaneous second- and third-order dispersion compensation in chirped-pulse amplification." In: *J. Opt. Soc. Am. B* 14.3 (Mar. 1997), pp. 661–665. DOI: 10.1364/JOSAB.14.000661. URL: http://josab.osa.org/abstract.cfm?URI=josab-14-3-661 (cit. on p. 41).

[20] Moeller Karl DIeter. *Optics: Learning by Computing, with Examples Using Mathcad?, Matlab?, Mathematica?, and Maple?* Springer Science+ Business Media, LLC, 2007 (cit. on p. 10).

[21] ML Landsman et al. "Light-absorbing properties, stability, and spectral stabilization of indocyanine green." In: *Journal of applied physiology* 40.4 (1976), pp. 575–583 (cit. on p. 57).

[22] *PubChem-Indocyanine green*. URL: https://pubchem.ncbi.nlm.nih.gov/compound/Indocyanine-green (visited on 04/23/2020) (cit. on p. 58).

[23] A. Rieznik et al. "Optimum Integration Procedures for Supercontinuum Simulation." In: *IEEE Photonics Journal* 4 (Apr. 2012), pp. 552–560. DOI: 10.1109/JPHOT.2012.2188281 (cit. on pp. 15, 18).

[24] Stephen D. Roberson and Paul M. Pellegrino. "Compression of Ultrafast Laser Beams." In: 2016 (cit. on pp. 27, 29).

[25] Alison Rodger. "Beer-Lambert Law Derivation." In: *Encyclopedia of Biophysics*. Ed. by Gordon C. K. Roberts. Berlin, Heidelberg: Springer Berlin Heidelberg, 2013, pp. 184–185. ISBN: 978-3-642-16712-6. DOI: 10.1007/978-3-642-16712-6_783. URL: https://doi.org/10.1007/978-3-642-16712-6_783 (cit. on p. 56).

[26] Schott. *Optical Glass Data Sheets*. In: 400 York Avenue, Duryea, PA 18642 USA: SCHOTT North America, Inc., 2017, p. 127. URL: https://www.schott.com/d/advanced_optics/ac85c64c-60a0-4113-a9df-23ee1be20428/1.14/schott-optical-glass-collection-datasheets-english-may-2019.pdf (visited on 2020) (cit. on p. 28).

[27] Jagdeep Shah. *Ultrafast spectroscopy of semiconductors and semiconductor nanostructures*. Vol. 115. Springer Science & Business Media, 2013, pp. 13–22 (cit. on p. 2).

[28] Steven A Soper and Quincy L Mattingly. "Steady-state and picosecond laser fluorescence studies of nonradiative pathways in tricarbocyanine dyes: implications to the design of near-IR fluorochromes with high fluorescence efficiencies." In: *Journal of the American Chemical Society* 116.9 (1994), pp. 3744–3752 (cit. on p. 56).

[29] Michael A. Sutton. "The Early History of Spectroscopy." In: *Johnson Matthey Technology Review* 32.1 (1988), p. 3. URL: https://www.technology.matthey.com/article/32/1/28-30/ (cit. on p. 1).

[30] R L Swofford and A C Albrecht. "Nonlinear Spectroscopy." In: *Annual Review of Physical Chemistry* 29.1 (1978), pp. 421–422. DOI: 10.1146/annurev.pc.29.100178.002225 (cit. on p. 2).

[31] Charles Thiel. "Four-Wave Mixing and its Applications." In: (Dec. 2000), pp. 1–2 (cit. on p. 13).

[32] Shanti Toenger et al. "Interferometric autocorrelation measurements of supercontinuum based on two-photon absorption." In: *JOSA B* 36.5 (2019), pp. 1320–1326 (cit. on p. 30).

[33] W. F. K. Wynne-Jones and Henry Eyring. "The Absolute Rate of Reactions in Condensed Phases." In: *The Journal of Chemical Physics* 3.8 (1935), pp. 492–502. DOI: 10.1063/1.1749713 (cit. on p. 1).

[34] Zahid Yaqoob et al. "Molecular contrast optical coherence tomography: A pump-probe scheme using indocyanine green as a contrast agent." In: *Journal of biomedical optics* 11 (Sept. 2006), p. 054017. DOI: 10.1117/1.2360525 (cit. on p. 63).